Electrocatalytic Activity of the 2D Monolayer of PtS₂ and Pt@PtS₂ Towards O₂ Reduction Reaction

M.Sc. Thesis

By **HARSHIT DUBEY**



DISCIPLINE OF PHYSICS INDIAN INSTITUTE OF TECHNOLOGY INDORE

May 2025

Electrocatalytic Activity of the 2D Monolayer of PtS₂ and Pt@PtS₂ Towards O₂ Reduction Reaction

A THESIS

Submitted in partial fulfillment of the requirements for the award of the degree of

Master of Science

by
HARSHIT DUBEY



DISCIPLINE OF PHYSICS INDIAN INSTITUTE OF TECHNOLOGY INDORE

May 2025



INDIAN INSTITUTE OF TECHNOLOGY INDORE

CANDIDATE'S DECLARATION

I hereby certify that the work which is being presented in the thesis entitled Electrocatalytic Activity of the 2D Monolayer of PtS₂ and Pt@PtS₂ Towards O₂ Reduction Reaction in the partial fulfillment of the requirements for the award of the degree of MASTER OF SCIENCE and submitted in the DISCIPLINE OF PHYSICS, Indian Institute of Technology Indore, is an authentic record of my own work carried out during the time period from July 2024 to May 2025 under the supervision of Dr. Srimanta Pakhira, Associate Professor, IIT Indore.

The matter presented in this thesis has not been submitted by me for the award of any other degree of this or any other institute.

Harshit Dubey 21/05/2025

Signature of the student with date (Harshit Dubey)

This is to certify that the above statement made by the candidate is correct to the best of my/our knowledge.

21.05.2025

Signature of the Supervisor of

M.Sc. thesis

(Dr. Srimanta Pakhira)

HARSHIT DUBEY has successfully given his M.Sc. Oral Examination held on

08/05/2025.

Signature of Supervisor of M.Sc. thesis

chila

Date: 21/05/2025

Convener, DPGC

Date: 22-05-25

ACKNOWLEDGEMENTS

I am deeply grateful to my thesis supervisor, Dr. Srimanta Pakhira, Associate Professor, for his invaluable guidance, unwavering support, insightful feedback, patience, and encouragement throughout the duration of my research work. His expertise and constructive feedback have been instrumental in shaping this thesis work.

I am deeply thankful to my lab group seniors, Mr. Vikash Kumar, Mr. Ashok Singh, Miss Himani Joshi, Miss Kahkasha Parveen, Mr. Dikeshwar Halba, Mr. Lokesh Yadav, Mr. Naveen Sharma, Mr. Anshuman Ojha, and Mr. Deepesh Jain, for their valuable discussions, continuous assistance and constant encouragement in every endeavor. Their expertise and support have greatly enriched this work, making this experience both enriching and enjoyable.

I am indebted to my parents for their unwavering love, encouragement, and understanding throughout this academic journey. Their encouragement and belief in me have been a constant source of my motivation. I am also grateful to my batchmates, Mr. Divyansh, Mr. Kuldeep, and Mr. Kartik, for always being present to provide any help possible.

Lastly, I would like to thank IIT Indore and the Department of Physics for providing me with the necessary opportunities to work and grow in this research endeavor.

ABSTRACT

The oxygen reduction reaction (ORR) is crucial in electrochemical energy conversion devices like fuel cells. Though vital to the performance of the fuel cell, it is very sluggish, highlighting the need for research focused on electrocatalysts and enhancing their effectiveness for developing high-activity and low-price electrocatalysts. In the same pursuit, this thesis computationally explored the ORR catalytic activity of the 2D monolayer PtS₂ and Pt atom anchored on the 2D monolayer PtS₂ (i.e., 2D monolayer Pt@PtS₂).

The first-principles density functional theory (DFT-D3) calculations have been employed to study the electronic, structural, and ORR catalytic properties of the 2D monolayer of PtS₂ and Pt@PtS₂. Electronic structure calculations revealed that the 1T PtS₂ monolayer has an indirect band gap of 2.97 eV, which reduces to an indirect band gap of 1.23 eV after the introduction of a Pt atom on the 2D monolayer PtS₂ (Pt@PtS₂), indicating the excellent electronic properties of the Pt@PtS₂ and its potential as an ORR electrocatalyst. In this thesis, the four-electron associative and dissociative reaction pathways were explored by calculating the adsorption energies (ΔE) of each of the intermediates involved. The dissociative pathway is found to be favorable for the 2D monolayer Pt@PtS₂, while the associative pathway is found to be favorable for 2D monolayer Pt@PtS₂. This study concludes that the 2D monolayer Pt@PtS₂ can act as an excellent ORR catalyst for the application in the fuel cells.

Table of Contents

Contents

Chapter 1: Introduction1					
Chapter 2: Density Functional Theory (DFT) Method5					
2.1: Many-Body Schrodinger Equation6					
2.2: Key Approximations in Many-Body Theory8					
2.2.1 Born-Oppenheimer Approximation8					
2.2.2 Independent Electrons Approximation8					
2.2.3 Mean-Field Approximation9					
2.3 Hartree-Fock Equations					
2.4: Kohn-Sham Equations11					
2.5: Self-Consistent Calculations12					
2.6: Conclusions and Limitations of DFT13					
Chapter 3: CRYSTAL2314					
Chapter 4: Theory and Computational Details16					
4.1: Theoretical Framework16					
4.2 Computational Details19					
Chapter 5: 2D Monolayer PtS ₂ 21					
5.1: Structural and Electronic properties					
5.2: ORR Catalytic Activity					
Chapter 6: 2D Monolayer Pt@PtS ₂ 35					
6.1: Structural and Electronic properties35					
6.2: ORR Catalytic Activity					
Chapter 7: Conclusions and Future Goals					

\mathbf{n}			NICO		4 4
к	нн	н к			41-
1.	171.1		11111	~~~~~~~~~~~~~~~~~~~~~~~~~~~~~~~~~~~~~~~	т.

List of Figures

Figure 1.1: A schematic diagram of the fuel cell2
Figure 2.1: Self-consistent solutions of the Kohn-Sham equations13
Figure 4.1: Schematic representation of the ORR pathways on the 2D PtS ₂ monolayer
surface17
Figure 5.1: Structural characteristics of the 1T phase of PtS ₂ 22
Figure 5.2: Structural characteristics of the 2H phase of PtS ₂ 23
Figure 5.3: (a) Band structure and (b) total DOS of 1T monolayer PtS ₂ 24
Figure 5.4: (a) Band structure and (b) total DOS of 2H monolayer PtS ₂ 244
Figure 5.5: Equilibrium geometries of all the intermediates involved during ORR in
both pathways for the 2D monolayer PtS ₂ 255
Figure 5.6: Relative adsorption energy diagram at the surface of the 2D monolayer PtS ₂
for (a) associative and (b) dissociative pathways during the ORR300
Figure 5.7: Spin-density plot for the (a) PtS ₂ and (b) O ₂ *_PtS ₂ 33
Figure 6.1: (a) Top view and (b) side view of the Pt atom anchored on the 2D monolayer
PtS ₂ (Pt@PtS ₂)
Figure 6.2: (a) Band structure and (b) DOS of the alpha spin Pt atom anchored on the
2D monolayer PtS ₂ (Pt@PtS ₂)
Figure 6.3: (a) Band structure and (b) DOS of both alpha and beta spins of the Pt atom
anchored on the 2D monolayer PtS ₂ (Pt@PtS ₂) 37
Figure 6.4: The side view of the equilibrium geometries of ORR intermediates of both
pathways for 2D monolayer Pt@PtS ₂ 38
Figure 6.5: Relative adsorption energy diagram at the surface of the 2D monolayer
Pt@PtS ₂ for (a) associative and (b) dissociative pathways during the ORR42

List of Tables

Table 5.1: Equilibrium structural characteristics of the bulk PtS2. 21
Table 5.2: The equilibrium configuration of the intermediate structures of 2D
monolayer PtS ₂ during ORR
Table 5.3: Adsorption energies (ΔE) for each ORR step of 2D monolayer PtS ₂ in the
associative pathway
Table 5.4: Adsorption energies (ΔE) for each ORR step of 2D monolayer PtS ₂ in the
dissociative pathway
Table 6.1: The equilibrium configuration of the intermediate structures of 2D
monolayer Pt@PtS2 during ORR
Table 6.2: Adsorption energies (ΔE) for each ORR step in the associative pathway for
2D monolayer Pt@PtS240
Table 6.3: Adsorption energies (ΔE) for each ORR step in the dissociative pathway for
2D monolayer Pt@PtS ₂ 411

Chapter 1: Introduction

The global energy demand has consistently increased in recent years, fueled by rapid population growth, increasing urbanization, and technological advancements. Currently, most of this demand is met by fossil fuels, which have been the dominant energy source. They currently supply almost 80 percent of the world's energy demand (Hosseini et al., 2023). While these fuels have enabled modern progress, their extensive use has resulted in numerous environmental challenges (Abdelkareem et al., 2021). When fossil fuels are burned, they release pollutants and greenhouse gases into the atmosphere, intensifying air pollution, global warming, and other forms of environmental degradation (S. Chu et al., 2016). Moreover, these fossil fuels are limited in stocks and are non-renewable energy sources. Thus, they will get depleted on the continuous extraction and usage. This has driven researchers around the globe to concentrate on developing sustainable and renewable energy sources.

While non-depleting sources like solar, wind, bioenergy, and hydroelectric power are available, their efficiency is affected by elements like meteorological state and seasonal shifts (Owusu et al., 2016). In this context, fuel cells present a promising alternative, which produces electricity through chemical processes, primarily using hydrogen as a fuel source. Unlike conventional combustion processes, the only byproducts of fuel cells are water and heat, making them a much cleaner option (Mekhilef et al., 2012). A diagram illustrating the fuel cell is shown in Figure 1.1 (Kulkarni et al., 2015).

In a fuel cell, hydrogen molecules (H₂) are broken down at the anode into protons (H⁺) and electrons (e⁻). The protons move through the proton exchange membrane (PEM) to the cathode while the electrons are routed through an external circuit, producing an electrical current. Upon reaching the cathode, the electrons combine with oxygen (O₂) and the protons to produce water (H₂O) as the byproduct, thereby closing the electrical circuit (*Grimes*, 1994). Thus, by harnessing the fuel cell technology, we can reduce our reliance on traditional energy sources, mitigate the harmful effects of pollution, and move toward a more sustainable energy future. The functioning of a fuel cell largely

depends on the cathodic oxygen reduction reaction (ORR), which is inherently sluggish. This slow reaction rate results in high overpotentials, significantly limiting the fuel cell's overall efficiency (Gewirth et al., 2010). To overcome the challenges posed by the ORR, researchers are exploring catalysts that can accelerate the kinetics of the ORR.

The key strategy for addressing the challenges associated with the sluggish ORR at the cathode is the development of more efficient catalysts. Catalysts are essential for lowering the activation energy required for the ORR, enhancing the reaction rate, and improving the overall fuel cell efficiency. Although platinum (Pt) and platinum-derived materials have traditionally been used (*Duan et al., 2013*), but their scarcity (which makes them a costly material) and poor stability hinder the commercialization of the

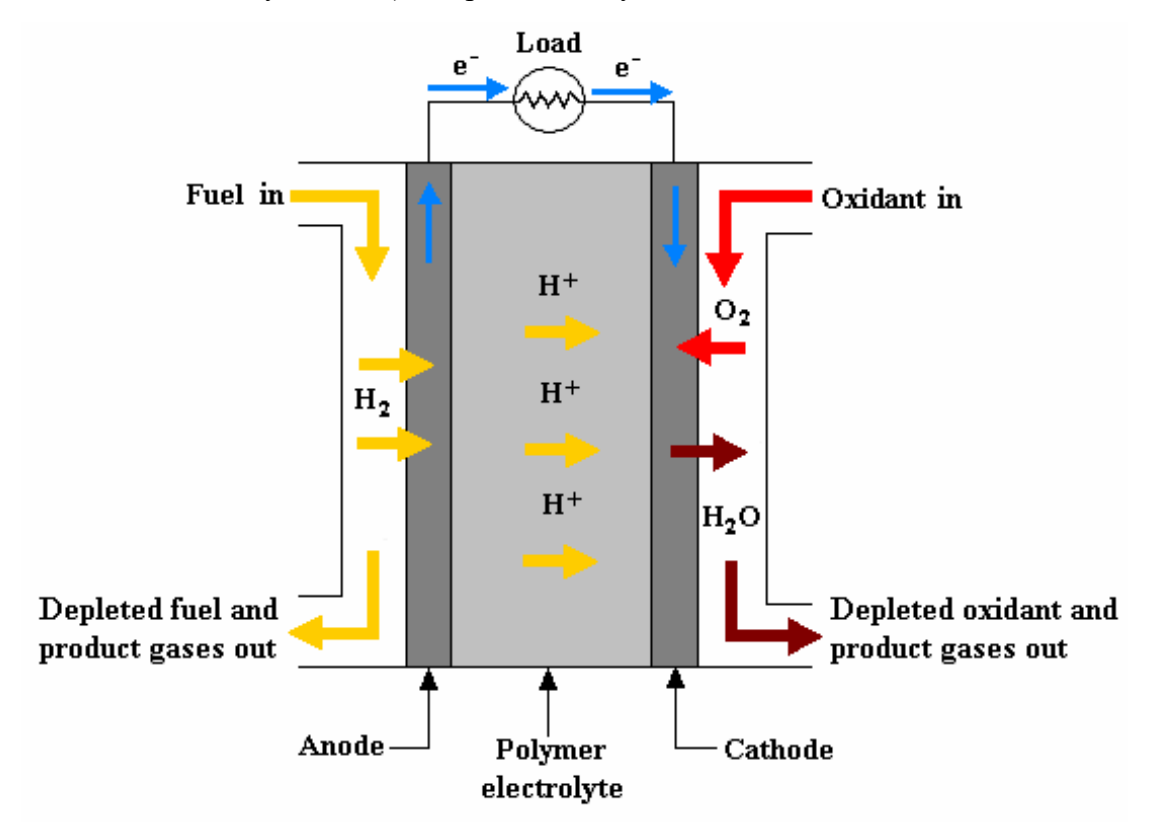


Figure 1.1. A schematic diagram of the fuel cell (*Kulkarni et al.*, 2015).

fuel cell. In addition to economic feasibility, the cathode material must fulfill specific criteria such as excellent thermal and electrical conductivity (*Hussain et al., 2020*). This has prompted the researchers to focus on developing more efficient catalysts.

Current trends in research have highlighted the substantial potential of two-dimensional materials as highly efficient catalysts because of their unique properties and high surface

area (Kumbhakar et al., 2023). These materials have high conductivity, excellent mechanical strength, and tunable electronic properties, which make them highly suitable for various catalytic applications. Among the various 2D materials, transition metal dichalcogenides (TMDs) have garnered significant attention as a promising alternative to platinum and platinum-based materials, owing to their high abundance and advantageous properties (Singh et al., 2024). These materials (2D TMDs) feature a layered structure with the chemical formula MX₂ (M is the transition metal atom, and X is the chalcogen atom). In TMDs, weak van der Waals forces hold the layers together, while strong covalent bonds link the atoms within each layer.

Among the numerous TMDs, 2D MoS₂ has gained significant attention for its excellent catalytic characteristics, which are comparable to those of Pt-based catalysts (Singh et al., 2024). Recent computational analysis have revealed that the 2D monolayer Pt-doped MoSe₂ demonstrates superior catalytic activity towards the ORR (Upadhyay et al., 2021). Previously, platinum dichalcogenides have been reported to exhibit good HER catalytic activity (Rosli et al., 2018).

Pt dichalcogenides offer significant advantages over Pt and Pt-based catalysts, particularly because of their 2D structure, which provides a high surface-to-volume ratio and a large number of catalytically active sites. This design reduces the amount of Pt needed, lowering overall costs. Furthermore, the improved stability and tunable electronic properties of these materials make them a cost-effective alternative for the ORR catalyst. Therefore, expanding research on the electrocatalytic performance of platinum dichalcogenides towards ORR is valuable. Also, when a single transition metal atom is anchored onto a Pt dichalcogenide monolayer, several advantages arise, such as an increase in the number of active sites, tuning of the electronic properties, and more (Back et al., 2018).

In the same pursuit, this work explores the structural and electronic characteristics, as well as the catalytic performance of the 2D monolayer PtS₂ and Pt atom anchored on the 2D monolayer of PtS₂ (Pt@PtS₂) for the ORR. To examine the catalytic activity of 2D monolayer platinum disulfide (PtS₂) and Pt@PtS₂ for the ORR, this study employs the first principles-based periodic hybrid density functional theory with the third-order

Grimme's dispersion correction, i.e., DFT-D3. By exploring their potential towards ORR, we aim to support the progress of more efficient and sustainable energy solutions.

Chapter 2: Density Functional Theory (DFT) Method

Density Functional Theory (DFT) method is a powerful and versatile quantum mechanical (QM) computational method primarily employed to calculate the electronic structure and properties of many-body systems. This theory can be further extended to determine the total energy of a system, reaction energies, thermodynamic quantities such as entropy and free energy, magnetic and optical properties, and a variety of other material properties. The DFT is a first principles (*ab initio*) approach that determines material properties based on fundamental physical principles, without requiring experimental data. This allows DFT to effectively model and study systems that have not been previously explored, which makes it an essential and crucial tool in both material science and molecular chemistry. This chapter discusses the fundamentals of DFT, including the many-body Schrödinger equation, the key approximations involved, the essential theorems, and the self-consistent field (SCF) approach.

The core idea of the DFT is rooted in the Hohenberg-Kohn (HK) theorem, which says that the electron density uniquely determines the energy of the ground state of a system. Unlike Hartree-Fock theory, which involves solving complex many-body wavefunctions, DFT simplifies the problem as it focuses on the electron density rather than the individual wave functions of the electrons. This approach effectively addresses the computational challenges associated with managing the electron-electron interactions in many-body systems, making it a convenient and practical framework for studying materials and molecules.

According to the DFT, the ground state energy (E) of a system is a functional of the electron density of the system only. Using this principle and the Hohenberg-Kohn theorem, the Kohn-Sham equations are solved using the self-consistent field approach to obtain the electronic structures. The computational methods for solving the Kohn-Sham equations have been employed in various software packages. The DFT is considered to be highly successful in calculating the equilibrium structures, vibrational properties and vibrational spectra, binding energy of the molecules, band structures of the metals and semiconductors. In light of its success and widespread application, it is

essential to acknowledge that DFT primarily focuses on describing the ground-state properties of materials and is not intended to describe electronic excitations or nonequilibrium phenomena.

Additionally, some properties of materials, such as the electronic band gaps of semiconductors and insulators, the electronic properties of Mott-Hubbard insulators, etc., cannot be calculated reliably using DFT. Therefore, the DFT cannot be expected to be a universal tool for calculating material properties.

2.1: Many-Body Schrödinger Equation

We consider the material to be a large and complicated collection of electrons and nuclei to study and understand their properties at the atomic scale. They hold together by having a balance between the attractive and the repulsive Coulombic interactions. The three kinds of Coulombic interactions that are considered in the material are as follows:

i. Repulsive interactions between the pairs of electrons: The energy associated with the repulsive interaction between two electrons at a distance d_{ee} is given below:

$$E_{ee} = \frac{e^2}{4\pi\epsilon_0 d_{ee}} \tag{2.1}$$

ii. Repulsive interactions between the pairs of nuclei: The repulsive energy between two nuclei with atomic number Z at a distance d_{nn} is given by:

$$E_{\rm nn} = \frac{Z^2 e^2}{4\pi\epsilon_0 d_{\rm nn}}$$
 (2.2)

iii. Attractive interactions between the electrons and the nuclei: The attractive energy between an electron and a nucleus at a distance d_{en} is given by:

$$E_{\rm ne} = -\frac{Ze^2}{4\pi\epsilon_0 d_{\rm en}} \tag{2.3}$$

To understand the behavior and the complete description of the quantum particles, the wavefunction $\psi(\mathbf{r})$ must be calculated throughout the region of interest. This is done by solving the Schrödinger equation for every point $r = xu_x + yu_y + zu_z$, where u_x , u_y , and u_z are the unit vectors along the Cartesian axes.

The time-independent Schrödinger equation is given by:

$$(\widehat{T} + \widehat{V})\psi = E\psi \tag{2.4}$$

where \widehat{T} and \widehat{V} represents the kinetic energy and the potential energy operator, E represents the energy eigenvalue of the system, and ψ is the corresponding wavefunction. Let us consider the system to be in equilibrium, i.e., the system is in its lowest energy state and is denoted by ψ_0 state and the corresponding equilibrium charge density is given by $|\psi_0|^2$.

To analyze the system having multiple electrons and multiple nuclei, we need to define the many body wavefunction ψ . This many body wavefunction is a function of the positions of all the electrons and nuclei within the system and is given by,

$$\psi(r_1, r_2, r_3, \dots, r_N; R_1, R_2, R_3, \dots, R_M)$$
 (2.5)

where $r_1, r_2, r_3, ..., r_N$ are the coordinates of the electrons of an N-electron system and $R_1, R_2, R_3, ..., R_M$ are the coordinates of the nuclei of an M-nuclei system.

The kinetic energy for such a system is given as,

Kinetic energy =
$$-\sum_{i=1}^{N} \frac{\hbar^2}{2m_e} \nabla_i^2 - \sum_{I=1}^{M} \frac{\hbar^2}{2M_I} \nabla_I^2$$
 (2.6)

The potential energy for the given system is given as,

(Potential energy)_{ee} =
$$\frac{1}{2} \sum_{i \neq j} \frac{e^2}{4\pi\epsilon_0} \frac{1}{|\mathbf{r}_i - \mathbf{r}_j|}$$
 (2.7)

(Potential energy)_{nn} =
$$\frac{1}{2}\sum_{I\neq J} \frac{e^2}{4\pi\epsilon_0} \frac{Z_I Z_J}{|\mathbf{R}_I - \mathbf{R}_I|}$$
 (2.8)

(Potential energy)_{en} =
$$-\sum_{i,I} \frac{e^2}{4\pi\epsilon_0} \frac{Z_I}{|\mathbf{r_i} - \mathbf{R_I}|}$$
 (2.9)

where the indices i and j run from 1 to N, I and J run from 1 to M. Thus, upon substituting the above written equations in the equation (2.4), the many-body Schrödinger equation is given by,

$$[-\sum_{i=1}^{N} \frac{\hbar^{2}}{2m_{e}} \nabla_{i}^{2} - \sum_{I=1}^{M} \frac{\hbar^{2}}{2M_{I}} \nabla_{I}^{2} + \frac{1}{2} \sum_{i \neq j} \frac{e^{2}}{4\pi\epsilon_{0}} \frac{1}{|\mathbf{r}_{i} - \mathbf{r}_{j}|} + \frac{1}{2} \sum_{I \neq j} \frac{e^{2}}{4\pi\epsilon_{0}} \frac{Z_{I}Z_{J}}{|\mathbf{R}_{I} - \mathbf{R}_{J}|} - \sum_{i,I} \frac{e^{2}}{4\pi\epsilon_{0}} \frac{Z_{I}}{|\mathbf{r}_{i} - \mathbf{R}_{I}|}] \psi = E_{tot} \psi$$
(2.10)

With the use of the Hartree atomic units, the above equation transforms into the following equation,

$$\left[-\sum_{i=1}^{N} \frac{\nabla_{i}^{2}}{2} - \sum_{I=1}^{N} \frac{\nabla_{I}^{2}}{2M_{I}} + \frac{1}{2} \sum_{i \neq j} \frac{1}{|\mathbf{r}_{i} - \mathbf{r}_{j}|} + \frac{1}{2} \sum_{I \neq j} \frac{Z_{I}Z_{J}}{|\mathbf{R}_{I} - \mathbf{R}_{I}|} - \sum_{i,I} \frac{Z_{I}}{|\mathbf{r}_{i} - \mathbf{R}_{I}|}\right] \psi = E_{tot} \psi \quad (2.11)$$

2.2: Key Approximations in Many-Body Theory

2.2.1 Born-Oppenheimer Approximation

In this, the nuclei are assumed to be held immobile (clamped) in known positions, and that the nuclei cannot move much. While this approximation may seem constrained, but it is a common occurrence. In the case of crystals, the nuclei are considered to be stationary, and their positions are determined with high accuracy through X-ray crystallography. This approximation is also known as clamped nuclei or adiabatic approximation.

Therefore, we will take the mass of each nucleus to be infinite, i.e., $M_I = \infty$, and according to it, we can neglect the kinetic energy of the nuclei in equation 2.11, and we can also take the Coulomb repulsion between nuclei to be a constant. Thus, on incorporating this assumption, the many-body Schrödinger equation becomes,

$$\left[-\sum_{i=1}^{N} \frac{\nabla_{i}^{2}}{2} + \frac{1}{2} \sum_{i \neq j} \frac{1}{|\mathbf{r}_{i} - \mathbf{r}_{i}|} - \sum_{i,I} \frac{Z_{I}}{|\mathbf{r}_{i} - \mathbf{R}_{I}|}\right] \psi = E \psi, \tag{2.12}$$

where
$$E=E_{tot}-\frac{1}{2}\sum_{I\neq J}\frac{Z_{I}Z_{J}}{|R_{I}-R_{I}|}.$$

We can take the nuclear coordinates, \mathbf{R}_I , as an external parameter, therefore, we can consider the ψ as a function of the electron coordinates, i.e., $\psi = \psi$ ($r_1, r_2, r_3, ..., r_N$). And, upon defining the Coulomb potential of the nuclei experienced by the electrons as,

$$V_{n}(r) = -\sum_{l} \frac{z_{l}}{|r-R_{l}|}$$
 (2.13)

the many-body Schrödinger equation can be written as,

$$\left[-\sum_{i=1}^{N} \frac{\nabla_{i}^{2}}{2} + \sum_{i} V_{n}(\mathbf{r}_{i}) + \frac{1}{2} \sum_{i \neq j} \frac{1}{|\mathbf{r}_{i} - \mathbf{r}_{j}|}\right] \psi = E \psi$$
 (2.14)

Thus, we can define the many-electron Hamiltonian as,

$$\widehat{H}(\mathbf{r}_{1}, \dots, \mathbf{r}_{n}) = -\sum_{i=1}^{N} \frac{\nabla_{i}^{2}}{2} + \sum_{i} V_{n}(\mathbf{r}_{i}) + \frac{1}{2} \sum_{i \neq j} \frac{1}{|\mathbf{r}_{i} - \mathbf{r}_{i}|}$$
(2.15)

2.2.2 Independent Electrons Approximation

To simplify the above-written complex equation, we further employ another approximation in which we assume that the electrons do not see each other to eliminate the term describing the Coulomb repulsion between electrons. Thus, the many-body Schrödinger equation becomes,

$$\sum_{i} \widehat{H}_{0}(\mathbf{r}_{i}) \psi = E \psi \tag{2.16}$$

$$\widehat{H}_0(\mathbf{r}) = -\frac{1}{2}\nabla^2 + V_n(\mathbf{r})$$
 (2.17)

where, $\widehat{H}_0(\mathbf{r})$ is the single particle Hamiltonian. The corresponding single-particle Schrödinger equation is given as follows,

$$\left[-\frac{1}{2}\nabla^2 + V_n(\mathbf{r})\right]\Phi_i(\mathbf{r}) = \varepsilon_i \Phi_i(\mathbf{r})$$
 (2.18)

As a result of this, we can write the wavefunction as,

$$\psi(\mathbf{r}_1, \mathbf{r}_2, ..., \mathbf{r}_N) = \phi_1(\mathbf{r}_1) ... \phi_N(\mathbf{r}_N)$$
 (2.20)

There are two significant drawbacks associated with the independent electrons approximation. The first drawback is that the wavefunction ψ should obey Pauli's exclusion principle as the electrons are fermions, but the above-written equation 2.20 does not hold this true. The second drawback is that the Coulomb term removed from the equation 2.11 is of the similar magnitude to the other terms, making it impossible to disregard.

In order to overcome the first drawback stated above, we can express the wavefunction $\psi(\mathbf{r}_1, \mathbf{r}_2, \dots, \mathbf{r}_N)$ as a Slater determinant. To overcome the second drawback, we make use of the mean-field approximation.

2.2.3 Mean-Field Approximation

As already mentioned in the above discussion that the approximation of ignoring the Coulomb repulsion between electrons in the many-body Schrödinger equation is too drastic. So, to maintain the single-particle description and to take account of the Coulomb repulsion in some form, we take the mean-field approximation.

According to the Poisson's equation, a distribution of electronic charge $n(\mathbf{r})$ will generate an electrostatic potential $\varphi(\mathbf{r})$ and we have,

$$\nabla^2 \varphi(\mathbf{r}) = 4\pi n(\mathbf{r}) \tag{2.21}$$

The potential energy of an electron immersed in this potential can be given as, $V_H(\mathbf{r}) = -\varphi(\mathbf{r})$, and is known as the 'Hartree potential'. Thus, we further have,

$$\nabla^2 V_{H}(\mathbf{r}) = -4\pi n(\mathbf{r}) \tag{2.22}$$

The solution to the above equation can be written as,

$$V_{H}(\mathbf{r}) = \int d\mathbf{r}' \frac{\mathbf{n}(\mathbf{r}')}{|\mathbf{r} - \mathbf{r}'|}$$
 (2.23)

The Hartree potential represents the average interaction each electron feels due to the others. As this includes averaging the individual effects, it is known as the mean-field approximation. The single-particle Hamiltonian is therefore, now given as,

$$\widehat{H}_0(\mathbf{r}) = -\frac{1}{2}\nabla^2 + V_n(\mathbf{r}) + V_H(\mathbf{r})$$
 (2.24)

and the single-particle Schrödinger equation is now given as,

$$\left[-\frac{1}{2}\nabla^2 + V_n(\mathbf{r}) + V_H(\mathbf{r})\right]\Phi_i(\mathbf{r}) = \varepsilon_i \Phi_i(\mathbf{r})$$
 (2.25)

$$\mathbf{n}(\mathbf{r}) = \sum_{i} |\phi_{i}(\mathbf{r})|^{2} \tag{2.26}$$

$$\nabla^2 V_{H}(\mathbf{r}) = -4\pi n(\mathbf{r}) \tag{2.27}$$

2.3: Hartree-Fock Equations

The main objective of the Hartree-Fock (HF) theory is to find out the single-particle ground state wavefunction. For this, we make use of the variational method to derive the Hartree-Fock equations by minimizing the ground state energy with respect to the single particle ground state wavefunction (*Harker*, 2016). Let us consider the quantum state ψ (trial wavefunction) that corresponds to the minimum energy, and therefore, the energy of this state can be obtained as follows,

$$E = \int d\mathbf{r}_1 \dots \dots d\mathbf{r}_N \psi^* \widehat{\mathbf{H}} \psi \qquad (2.28)$$

On minimizing the energy w.r.t. $\phi_i(\mathbf{r})$ and requiring the orthonormality of the wavefunctions $\phi_i(\mathbf{r})$ provides us the necessary equations governing their behavior. These equations are also known as Hartree-Fock equations and are written below,

$$\left[-\frac{\nabla^2}{2} + V_n(\mathbf{r}) + V_H(\mathbf{r}) \right] \phi_i(\mathbf{r}) + \int d\mathbf{r}' V_X(\mathbf{r}, \mathbf{r}') \phi_i(\mathbf{r}') = \epsilon_i \phi_i(\mathbf{r})$$
 (2.29)

$$\mathbf{n}(\mathbf{r}) = \sum_{i} |\phi_{i}(\mathbf{r})|^{2} \tag{2.30}$$

$$\nabla^2 V_H(\mathbf{r}) = -4\pi n(\mathbf{r}) \tag{2.31}$$

By comparing the above three equations with equations 2.25-2.27, we obtain an additional potential, V_X . This potential is known as the Fock exchange potential, which emerges from the requirement that no two electrons can occupy the same quantum state, in accordance with Pauli's exchange principle. This potential has been introduced to take care of the quantum nature of the electrons. The expression for the Fock-exchange potential has been given below,

$$V_{X}(\mathbf{r}, \mathbf{r}') = -\sum_{j} \frac{\phi_{j}^{*}(\mathbf{r}')\phi_{j}(\mathbf{r})}{|\mathbf{r} - \mathbf{r}'|}$$
(2.32)

2.4: Kohn-Sham Equations

This section discusses the correlation between the electrons and the Kohn-Sham formalism. Due to Coulomb repulsion, the probability of locating an electron in a given region decreases when other electrons are nearby, suggesting that our trial wavefunction may not be entirely precise. To incorporate this effect, we add an extra potential term to the potential $V_n + V_H + V_X$ in the single-particle equations. This extra potential is known as the correlation potential and is denoted by $V_c(\mathbf{r})$. Thus, we arrive at the following single-particle equation:

$$\left[-\frac{1}{2}\nabla^2 + V_n(\mathbf{r}) + V_H(\mathbf{r}) + V_x(\mathbf{r}) + V_c(\mathbf{r})\right]\Phi_i(\mathbf{r}) = \varepsilon_i \Phi_i(\mathbf{r})$$
 (2.33)

The Kohn-Sham equations reformulate the many-body problem of interacting electrons into a set of single-particle equations by introducing an effective potential that incorporates both external and electron-electron interactions. This approach forms the basis of the DFT, simplifying the electronic structure calculations with good accuracy. The Hohenberg-Kohn theorem tells us that the total energy of a system of many electrons in their ground state is a functional of the electron density (Epstein et al., 2001; Hohenberg et al., 2018). This theorem provides the basis for the DFT as it is the theoretical foundation for finding the energy and properties of a system. We have the following functional for the ground state energy calculation,

$$\mathcal{F}[\mathbf{n}] = \int d\mathbf{r} \, \mathbf{n}(\mathbf{r}) V_{\mathbf{n}}(\mathbf{r}) + \langle \Psi(\mathbf{n}) | \widehat{\mathbf{T}} + \widehat{\mathbf{W}} | \Psi(\mathbf{n}) \rangle \tag{2.34}$$

Rewriting the above functional by decomposing the last two terms depending implicitly on the electron density, we get,

$$E = \mathcal{F}[n] \tag{2.35}$$

$$E = \int d\mathbf{r} \mathbf{n}(\mathbf{r}) V_{\mathbf{n}}(\mathbf{r}) - \sum_{i} \int d\mathbf{r} \phi_{i}^{*}(\mathbf{r}) \frac{\nabla^{2}}{2} \phi_{i}(\mathbf{r}) + \frac{1}{2} \iint d\mathbf{r} d\mathbf{r}' \frac{\mathbf{n}(\mathbf{r})\mathbf{n}(\mathbf{r}')}{|\mathbf{r} - \mathbf{r}'|} + E_{xc}[n] \quad (2.36)$$

The first term of the above expression represents the contribution to the total energy by the external potential, the second term represents the kinetic energy, the third term represents the Hartree energy, and the last term represents everything left out and is known as exchange and correlation energy. The exchange and correlation functional is given by Eq. 2.39 and the Kohn-Sham equations are given below:

$$\left[-\frac{1}{2} \nabla^2 + V_{\text{tot}}(\mathbf{r}) \right] \phi_i(\mathbf{r}) = \epsilon_i \phi_i(\mathbf{r})$$
 (2.37)

$$V_{\text{tot}}(\mathbf{r}) = V_{\text{n}}(\mathbf{r}) + V_{\text{H}}(\mathbf{r}) + V_{\text{xc}}(\mathbf{r})$$
 (2.38)

$$V_{n}(\mathbf{r}) = -\sum_{I} \frac{Z_{I}}{|\mathbf{r} - \mathbf{R}_{I}|}$$
 (2.39)

$$\nabla^2 V_{H}(\mathbf{r}) = -4\pi n(\mathbf{r}) \tag{2.40}$$

$$V_{xc}(\mathbf{r}) = \frac{\delta E_{xc}[n]}{\delta n}(\mathbf{r})$$
 (2.41)

$$\mathbf{n}(\mathbf{r}) = \sum_{i} |\phi_{i}(\mathbf{r})|^{2} \tag{2.42}$$

2.5: Self-Consistent Calculations

Self-consistency means that after repeating the steps of a calculation, we get the same results with which we had begun the calculation, showing that the process has converged and reached a steady state, and further repetitions do not lead to any changes.

The solution to the Kohn-Sham equations begins with the calculation of the total potential, V_{tot}, which comprises the nuclear potential, V_n, the Hartree potential, V_H, and the correlation and exchange potential, V_{xc}. The nuclear potential, V_n, does not depend on the electron density, $n(\mathbf{r})$, and is calculated by specifying the nuclear coordinates. This information is obtained from the crystallographic data, which contains the atomic coordinates required to describe the structure of the material. The Hartree potential, V_H, and the correlation and exchange potential, Vxc, depends on the electron density. To begin, we approximate the electron density $n(\mathbf{r})$ by summing the electron densities of the completely isolated atoms, placed according to the atomic positions of the material being studied. The potentials V_H, V_{xc}, and V_{tot} are calculated using this initial density. The Kohn-Sham equations are solved from the total potential to obtain a new set of wavefunctions. These wavefunctions are then used to generate an improved estimate of the electron density, which is used to update the total potential. The process of solving the Kohn-Sham equations, updating the density and the potential, and evaluating the changes is carried out repeatedly until the new density matches the old density with the desired level of tolerance. When the condition of the desired tolerance is met, we say that we have achieved self-consistency. The schematic flow for the self-consistent solutions is shown in Figure 2.1.

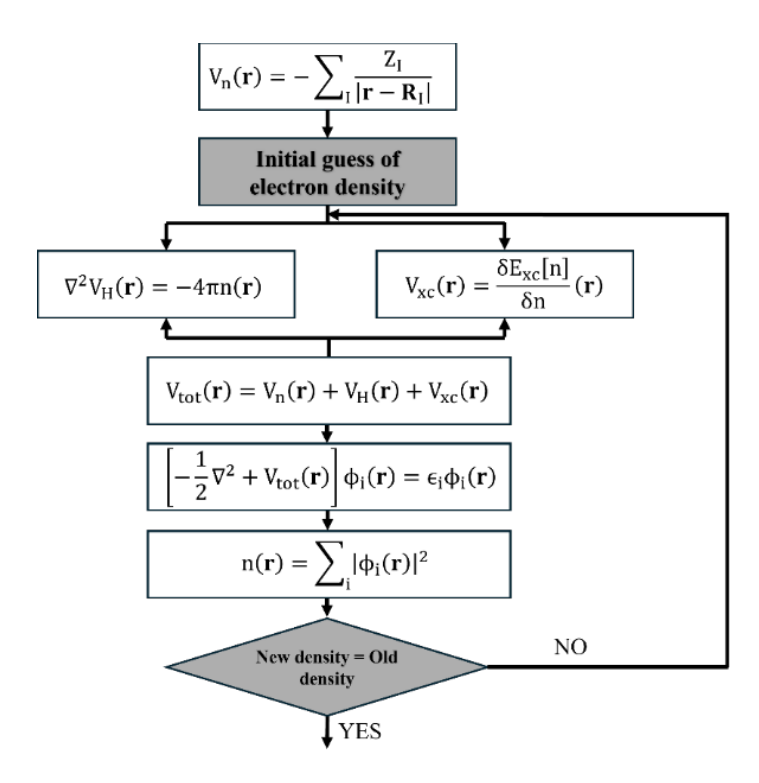


Figure 2.1. Self-consistent solutions of the Kohn-Sham equations (*Harker*, 2016).

2.6: Conclusions and Limitations of DFT

DFT has helped us to transform the way we investigate the electronic structure of atoms, molecules, and solids. It is one of the most widely used methods in computational physics and chemistry because of its ability to handle complex quantum systems, versatility, and reliability. While DFT performs with good accuracy for predicting equilibrium geometries, reaction energies and mechanisms and vibrational properties, it is not a reliable tool for the calculation of the electronic band gaps of semiconductors and insulators, it does not accurately describe van der Waals interactions without the corrections and is not well suited for the excited state phenomena.

Chapter 3: CRYSTAL23

All the calculations presented in this thesis were performed by the CRYSTAL23 software (*Erba et al.*, 2023). It is a powerful and versatile computational tool used for performing the density functional theory calculations. It is designed to simulate the electronic structure and properties of periodic solids. This software incorporates both the Hartree-Fock and Kohn-Sham formulations for the electronic structure calculations within the framework of density functional theory. It allows for the inclusion of a wide range of exchange-correlation functionals, enabling accurate treatment of electron correlation effects. The program uses localized Gaussian-type basis sets to handle periodic solids.

CRYSTAL is designed to manage systems with different dimensions within a unified and consistent framework. It can effectively handle one-dimensional polymers, two-dimensional slabs, three-dimensional crystalline solids, and zero-dimensional molecules. The software is based on the representation of single-particle wave functions, known as crystalline orbitals. These orbitals are expressed as linear combinations of Bloch functions, which themselves are formed from localized atomic orbitals. The atomic orbitals are expressed as linear combinations of Gaussian-type functions. Depending on the chemical elements involved, users can specify symmetry-adapted basis sets that may contain s, p, d, and f orbitals.

A key feature of CRYSTAL is its automatic treatment of symmetry. The software supports a comprehensive range of symmetry groups, including all 230 space groups, 80 layer groups, 99 rods groups, and 45 point groups. Its input options allow for the construction of lower-dimensional structures such as slabs (2D), nanorods (1D), and clusters (0D) directly from the three-dimensional crystal data. These capabilities significantly broaden the range of systems that can be investigated, making CRYSTAL a versatile tool for the study of materials with periodic, reduced-dimensional, or complex geometries.

The input file structure of CRYSTAL23 has been shown below by taking the example of the 2D monolayer PtS₂.

2D Monolayer PtS ₂	#Title Line
SLAB	#Dimensionality of the system
72	#Layer group (P-3m1; 164)
3.5487 3.5487 120	#Lattice parameters
2	#Number of atoms in the system
278 0.00000 0.00000 0.000000000	#Atomic number and coordinates
16 0.33333 0.66667 1.233234917	#Atomic number and coordinates
OPTGEOM	
FULLOPTG	
MAXCYCLE	#Keywords related to
800	geometry optimization
ENDOPT	
END	
#Basis sets of all the atoms of the structure	
END	#End of basis set input section
SHRINK	#Reciprocal space integration
parameters	
0 30	
#Optional keywords	
END	#End of SCF input section

Chapter 4: Theory and Computational Details

4.1: Theoretical Framework

The fuel cell directly converts the chemical energy of the fuel to electrical energy, having byproducts such as water (H₂O) and heat, making it environment-friendly compared to traditional energy sources like fossil fuels, which emit CO₂, CO, CH₄, and other pollutants. In the hydrogen fuel cell, hydrogen gas (H₂) is introduced to the anode, where it decomposes into protons (H⁺) and electrons (e⁻) (Felseghi et al., 2019; Maheshwari et al., 2018), and the corresponding anodic reaction is given as follows:

$$H_2 \longrightarrow 2H^+ + 2e^-$$

The H⁺ ions travel through the PEM to reach the cathode, while the electrons flow through the external electrical circuit before arriving at the cathode side. The flow of electrons from the anode to the cathode through the external circuit generates electrical power. At the cathode, O₂ undergoes reduction by combining with the protons and electrons, producing water and heat as the final product (*Maheshwari et al.*, 2018). The corresponding cathodic reaction is given as follows:

$$2H^+ + \frac{1}{2}O_2 + 2e^- \longrightarrow H_2O$$

Thus, the overall redox reaction is given as:

$$2H_2 + O_2 \longrightarrow 2H_2O$$

The ORR occurring at the cathode is vital for the functioning of the fuel cell. In an acidic medium, the ORR typically proceeds through one of two pathways: the four-electron (4e⁻) reduction pathway or the two-electron reduction pathway (*Dange et al., 2022; Nie et al., 2015*). The four-electron reduction (direct reduction) of the O₂ molecule is given as follows:

$$O_2 + 4H^+ + 4e^- \longrightarrow 2H_2O;$$
 $E^0 = 1.23 \text{ eV}$

The two-electron reduction (indirect reduction) of the O₂ molecule is as given below:

$$O_2 + 2H^+ + 2e^- \longrightarrow H_2O_2;$$
 $E^o = 0.68 \text{ eV}$ $H_2O_2 + 2H^+ + 2e^- \longrightarrow 2H_2O;$ $E^o = 1.77 \text{ eV}$

In fuel cell applications, the four-electron (4e⁻) reduction pathway is favored as it prevents hydrogen peroxide formation, improves efficiency, and enhances the overall

functionality of the fuel cell (*Gewirth et al.*, 2010). Furthermore, the 4e⁻ reduction in the acidic medium is classified into two distinct types, depending on the mechanism by which the O=O bond is cleaved during the reduction process. These are the associative pathway and the dissociative pathway, and are discussed as follows:

(i) Associative pathway: In the associative pathway, oxygen (O₂) is first adsorbed on the catalyst surface to form O₂* intermediate, then it reacts with H⁺ and e⁻, arriving from the anodic side, resulting in the formation of OOH* species. This intermediate subsequently reacts with another H⁺ and e⁻ and gets converted into O* intermediate with the evolution of a water molecule, and the O* again combines with the H⁺ and e⁻ coming from the anodic side and gets converted into OH* intermediate. The OH* further reacts with H⁺ and e⁻ to form H₂O, and finally, the desorption of the water molecules occurs from the catalyst's surface. The step-by-step 4e⁻ reduction process is presented below:

$$0_{2} + * \longrightarrow 0_{2}^{*}$$

$$0_{2}^{*} + (H^{+} + e^{-}) \longrightarrow 00H^{*}$$

$$00H^{*} + (H^{+} + e^{-}) \longrightarrow 0^{*} + H_{2}0$$

$$0^{*} + (H^{+} + e^{-}) \longrightarrow 0H^{*}$$

$$0H^{*} + (H^{+} + e^{-}) \longrightarrow H_{2}0 + *$$

where * represents the active site of the catalyst.

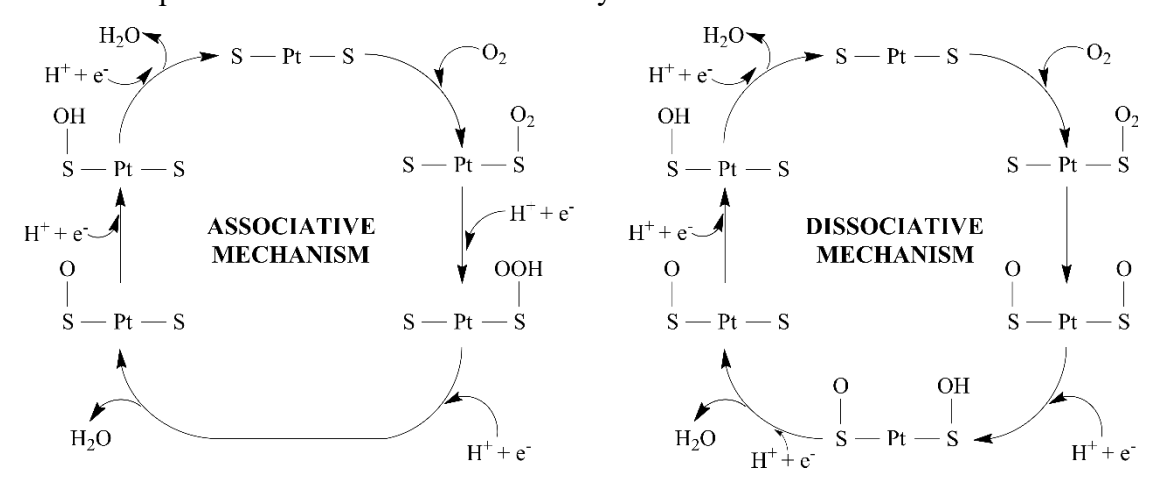


Figure 4.1. Schematic representation of the ORR pathways on the 2D monolayer PtS₂ surface.

(ii) Dissociative pathway: In the dissociative pathway, after O₂ is adsorbed on the surface of the catalyst, the O=O bond breaks down, forming O* species. These O* species undergo reaction with the H⁺ and e⁻ to produce OH*, which, upon further

reaction with the H⁺ and e⁻, gets transformed into a water molecule and gets desorbed from the catalyst's surface. Below is a breakdown of the reaction steps involved:

$$0_{2}^{*} \longrightarrow 20^{*}$$

$$20^{*} + (H^{+} + e^{-}) \longrightarrow 0H^{*} + 0^{*}$$

$$0H^{*} + 0^{*} + (H^{+} + e^{-}) \longrightarrow 0^{*} + H_{2}0$$

$$0^{*} + (H^{+} + e^{-}) \longrightarrow 0H^{*}$$

$$0H^{*} + (H^{+} + e^{-}) \longrightarrow H_{2}0 + *$$

In the present work, the catalytic activity of the 2D monolayer Pt_2 and 2D monolayer Pt_2 for ORR is determined by computing the adsorption energy of intermediates at each stage of the reaction (*Huang et al., 2021*). The adsorption energy has been denoted by ΔE and is defined by the following equation:

$$\Delta E = E_{adsorbate+adsorbent} - E_{adsorbate} - E_{adsorbent}$$
 (4.1)

where the E_{adsorbate+adsorbent}, E_{adsorbate}, and E_{adsorbent} are the total energy for the adsorbed system, adsorbate, and adsorbent, respectively.

The negative adsorption energy means that the energy will be released in the reaction and therefore indicates the stability of the adsorbed species on the adsorbent system as a result of the adsorption. Thus, the nature of the reaction will be exothermic, and the process is energetically favorable. On the other hand, the positive value of adsorption energy means that energy needs to be supplied to make the reaction happen. Therefore, the reaction will be endothermic and is energetically unfavorable.

4.2: Computational Details

In our study, we applied the computational hydrogen electrode (CHE) method to calculate the adsorption energy of each of the intermediates. This method is based on the standard conditions, which uses the approach developed by Nørskov et al., which revealed that the chemical potential of a proton-electron pair (H⁺ + e⁻) is related to $\frac{1}{2}$ H₂ in the gas phase. By using this relationship, we were able to calculate the energy change for the reaction X + H \rightarrow X + H⁺ + e⁻ by referencing the reaction X + H \rightarrow X + $\frac{1}{2}$ H₂ (Nørskov et al., 2004).

All the findings (i.e., equilibrium structure with the corresponding electronic properties and energetics) of this study have been carried out by employing the first principles-based hybrid density functional theory (DFT-D3) method implemented in the CRYSTAL23 suite package (*Erba et al., 2023*). For improved accuracy, we have incorporated the weak van der Waals interactions by including the third-order Grimme's dispersion corrections (i.e., "-D3") along with the B3LYP functional, i.e., all the DFT calculations have been carried out by employing the hybrid B3LYP-D3 functional (*Chen et al., 2006; Grimme et al., 2010*). We used the "FMIXING" parameter to control the mixing of the FOCK and Kohn-Sham matrices when applying the hybrid functional. To ensure the accuracy of our calculations, we set the matrix mixing to 90%. When using hybrid functionals, it is crucial to carefully regulate the interaction between the Fock and Kohn-Sham matrices during the self-consistent field iterations. By fine-tuning this mixing percentage, we achieve an effective balance between the exact exchange term and the Kohn-Sham functional. The choice of 90% mixing has been applied to ensure both the precision of the results and computational efficiency.

We have computationally constructed the 2D monolayer slab of PtS₂ by cleaving the (0 0 1) surface from the bulk PtS₂, and the 2D monolayer Pt@PtS₂ was constructed by adding a Pt atom onto the top of the surface of the 2D monolayer PtS₂. To explore the electronic properties and determine the equilibrium structures during the periodic hybrid DFT-D3 calculations, we conducted spin-polarized calculations by assigning the electron occupancy for the alpha (up-spin) and beta (down-spin) states. The calculations were carried out using the keywords "ATOMSPIN" and "SPINLOCK" in the CRYSTAL23 suite package. In this work, triple-ζ valence polarized (TZVP) Gaussian-

type basis sets were utilized to describe the atomic orbitals of Pt, S, O and H atoms (Tosoni et al., 2007; Vilela Oliveira et al., 2019). For the integration in the first Brillouin zone, a 4×4×1 k-point mesh under the Monkhorst-Pack scheme was used for the geometry optimization (Monkhorst et al., 1976). To ensure the absence of any possible interactions among the repeated replicas of the monolayer slab, we imposed a 500 Å vacuum gap in the perpendicular z-direction of the 2D monolayer surfaces (Singh et al., 2023). The self-consistent field (SCF) calculations were considered to be converged when the energy difference between the two successive iterations reached 10⁻⁷ atomic units (a.u.).

The maximum and RMS force criteria are specified as 0.000450 a.u. and 0.000300 a.u., respectively, while the maximum and RMS displacement criteria are specified as 0.001800 a.u. and 0.001200 a.u., respectively. To examine the electronic properties of the material, the band structure was computed and displayed along the high-symmetrical Γ -M-K- Γ k-path within the irreducible Brillouin zone. The visualization program VESTA is used to design all the structures involved in this study (Momma et al., 2011). It has also been used to visualize all the equilibrium configurations and their atomic arrangements and to create their corresponding images.

Chapter 5: 2D Monolayer PtS₂

5.1: Structural and Electronic Properties

The 2D monolayer PtS_2 mainly occurs in two phases namely 1T and 2H phase. In this work, we have considered both the 1T and 2H phases of the 2D monolayer PtS_2 as an electrocatalyst for ORR. In this work, we obtained the equilibrium structure of both phases using the dispersion-corrected hybrid DFT (B3LYP-D3). The structure has $P\overline{3}m1$ layer group symmetry.

1T Phase: In the 1T phase of the 2D monolayer PtS_2 , one Pt atom is surrounded in octahedral coordination by the S atoms, as shown in Figure 5.1 (e). The lattice parameters a = b = 3.53 Å and $\gamma = 120^{\circ}$ have been used to characterize the equilibrium structure, which closely matches the previously mentioned values (*Yin et al., 2022*). Figures 5.1 (a) and (b) show their top and side views, respectively. It has a stacking sequence of the ABCABCABC... type, as represented in Figure 5.1 (d).

2H Phase: In the 2H phase of the 2D monolayer PtS₂, one Pt atom is trigonal prismatic coordinated by six S atoms, as shown in Figure 5.2 (e). The lattice parameters a = b = 3.41 Å and $\alpha = \beta = 90^{\circ}$, $\gamma = 120^{\circ}$ characterize the configuration of the equilibrium structure. Figures 5.2 (a) and 5.2 (b) show their top and side views. This phase has a stacking sequence of the ABABAB... type.

Table 5.1. Equilibrium structural characteristics of the bulk PtS₂.

System	Lattice parameters	Interfacial angle	Symmetry	Average bond	References
	$a = b (\mathring{A})$	γ (°)		Length of Pt-S	
1T PtS ₂	3.53 Å	120°	P3m1	2.41 Å	This work
1T PtS ₂	3.56 Å	120°	P3̄m1	2.39 Å	(Yin et al., 2022)
2H PtS ₂	3.41 Å	120°	P3̄m1	2.45 Å	This work

The transfer of electrons is essential to the ORR, significantly influencing both reaction kinetics and overall efficiency. The band structure and density of states (DOS) are essential electronic characteristics of catalysts that significantly influence their catalytic activity. By understanding and optimizing these characteristics, we can enhance the

performance of catalysts, leading to improvements in various applications, including fuel cells and other electrochemical systems. The electronic characteristics of both phases have been investigated by analyzing their electronic band structure and total DOS. For each case, the band structure is presented following the high symmetry k-path Γ -M-K- Γ , referenced to the vacuum level, as shown in Figure 5.3 and Figure 5.4.

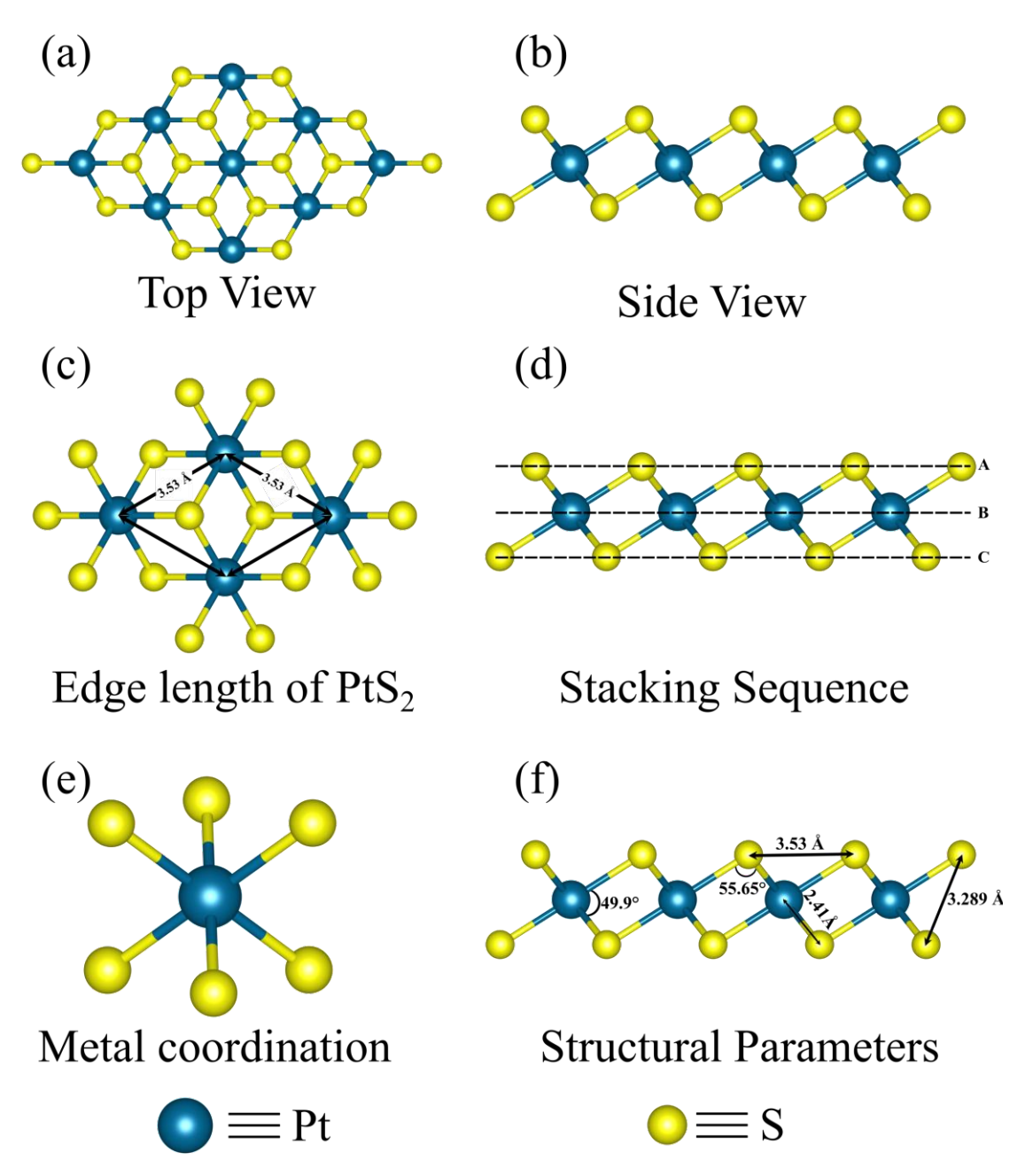


Figure 5.1. Structural characteristics of the 1T phase of PtS₂.

The 1T phase has a Fermi energy level (E_F) of -5.29 eV, whereas the 2H phase exhibits a slightly higher E_F value of -4.93 eV. The 1T phase of 2D monolayer PtS₂ exhibits a band gap of 2.97 eV, indicating its semiconducting behavior, while the 2H phase of PtS₂ is found to be metallic in nature.

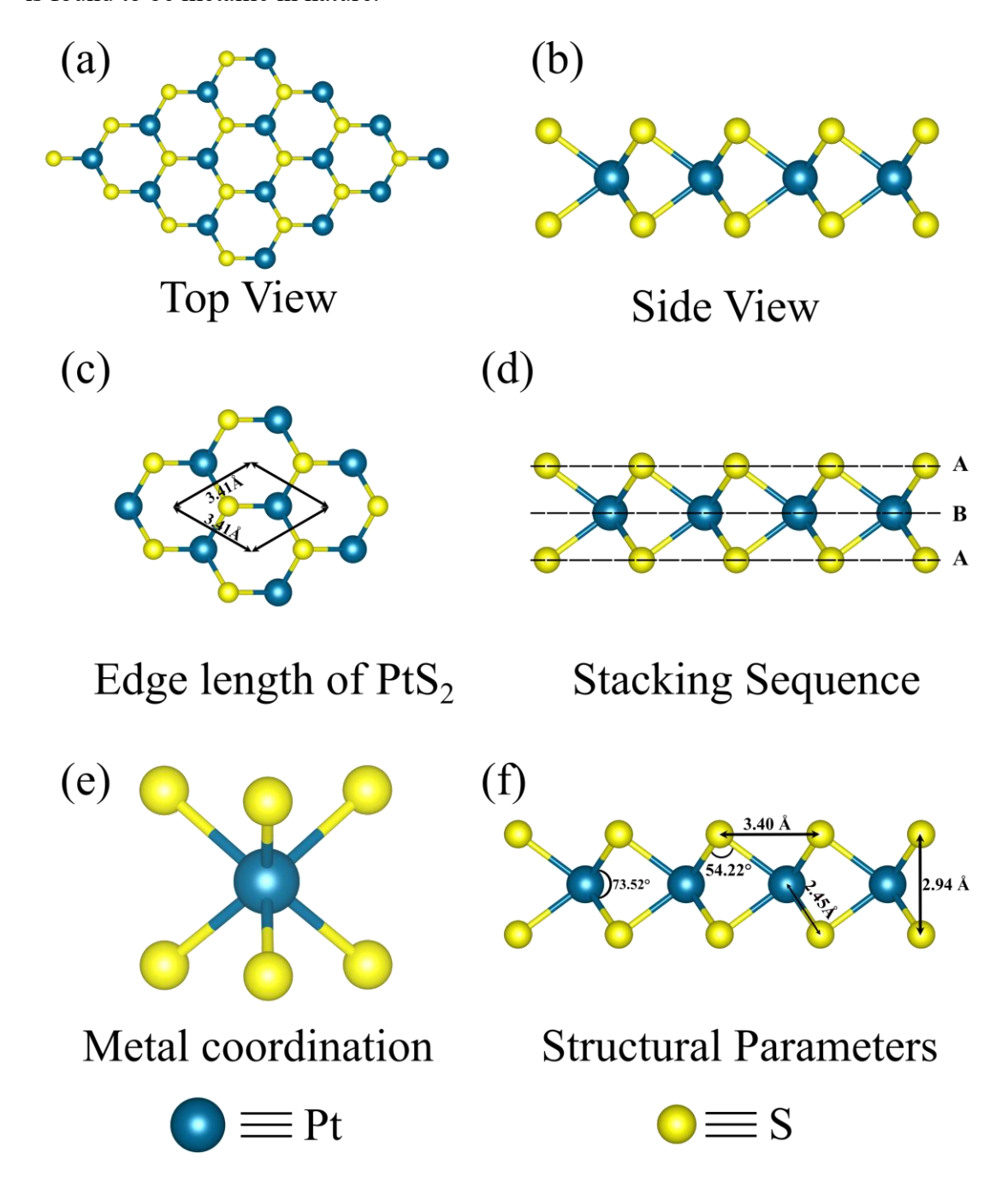


Figure 3.2. Equilibrium structural characteristics of 2H phase of PtS₂.

We found out that the 1T-PtS₂ is thermodynamically more stable than its 2H phase (Sun et al., 2025). The enhanced stability of the 1T phase will facilitate a more robust and efficient catalytic environment, thereby potentially offering superior ORR performance compared to the less stable 2H phase. Therefore, the subsequent analysis of the 2D monolayer PtS₂ for ORR catalysis is focused on the 1T phase.

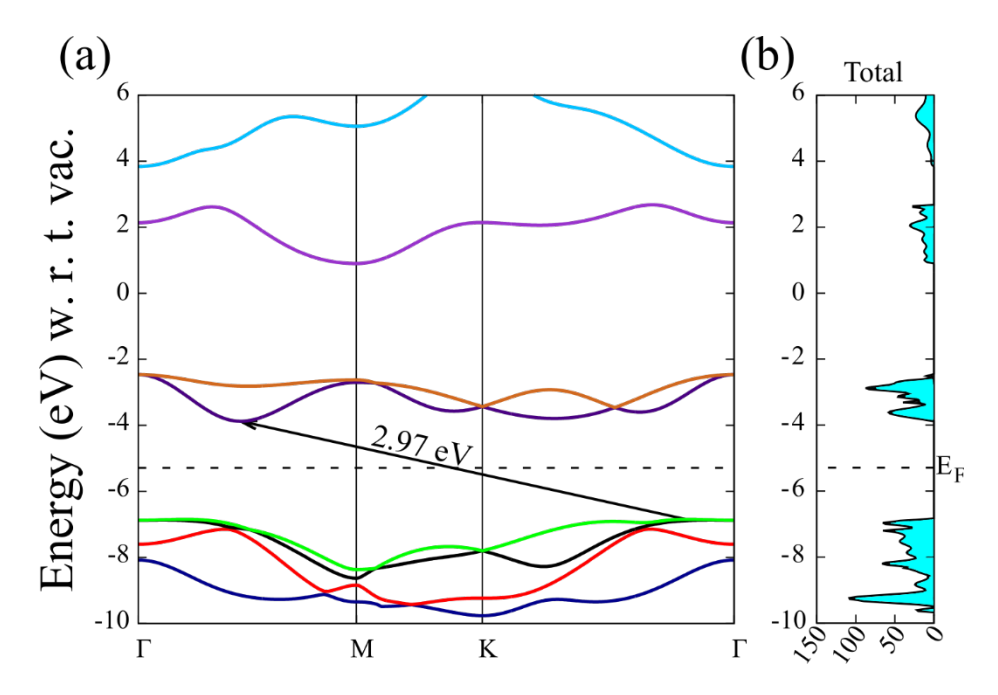


Figure 5.3. (a) Electronic Band structure and (b) total DOS of 1T monolayer PtS₂.

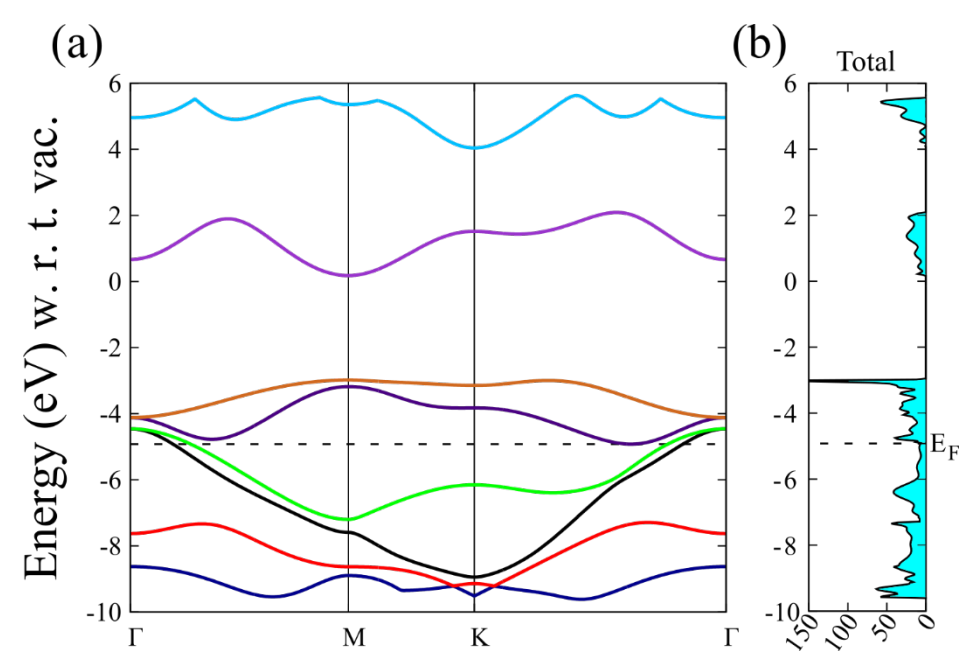


Figure 5.4. (a) Electronic band structure and (b) total DOS of 2H monolayer PtS₂.

In this work, a 2×2 supercell of the 1T phase of the 2D monolayer PtS₂ was computationally designed using the VESTA software. The equilibrium geometry was obtained using the DFT-D3 method, and its top and side view is shown in Figure 5.1 (a) and (b). In this study, we examined the ORR activity of the 2D monolayer PtS₂ in an acidic medium. The S atoms on the exposed surface of the Pt dichalcogenides serve as the active site for the catalysis of the ORR. This work investigates the ORR performance by considering the S atoms as the active sites. The first step of the ORR mechanism involves the adsorption of the O₂ molecule, which can further proceed via two distinct

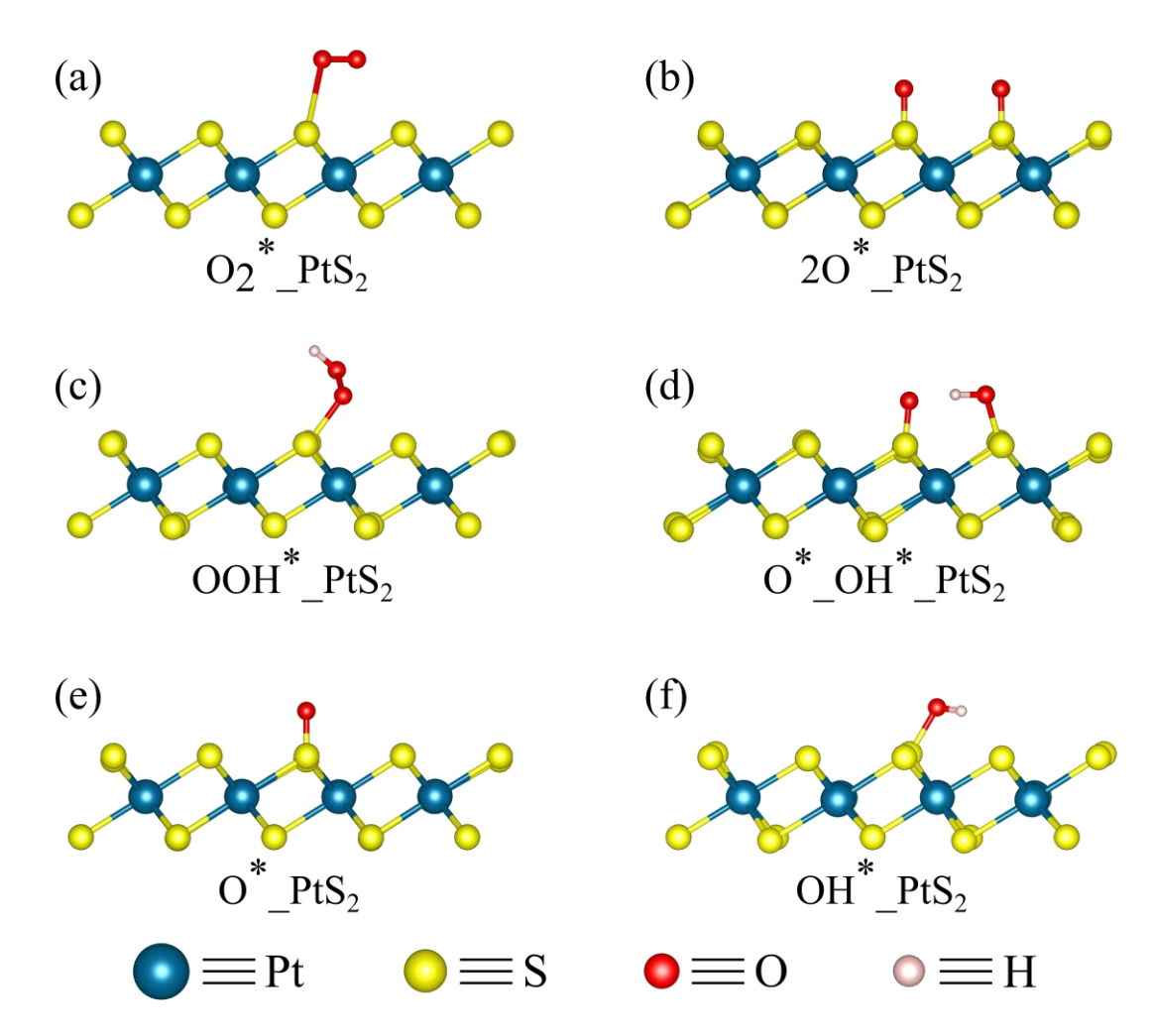


Figure 5.5. Equilibrium geometries of all the intermediates involved during ORR in both pathways for the 2D monolayer PtS_2 .

pathways, depending on how the O=O bond dissociates. The first way is known as the associative pathway, which involves the formation of the OOH* species through the addition of an electron-proton pair $(H^+ + e^-)$ coming from the anodic side to the O₂. The

OOH* intermediate further reacts with another pair of an electron and a proton and is reduced to the O* intermediate with the evolution of a water molecule. The O* intermediate on the successive addition of the electron-proton pairs restores the catalyst to its initial state with the evolution of another water molecule, and the reaction intermediates involved in the associative mechanism are given by the following steps: * (active site of the catalyst) \rightarrow O2* \rightarrow OOH* \rightarrow OH* \rightarrow *. Once the catalyst has been restored to its initial state, it is now ready to facilitate the additional cycles of the ORR.

Table 5.2. The equilibrium configuration of the intermediate structures of 2D monolayer PtS₂ during ORR.

Reaction	Lattice parameters (Å)		Interfacial angle (°)		Symmetry	Average bond length in Å		
Steps								
	a	b	α=β	γ		Pt-S	S-O	S-OH
PtS ₂	7.06	7.06	90	120	P1	2.41	-	-
O2*_PtS2	7.06	7.05	90	119.94	P1	2.41	2.78	-
2O*_PtS ₂	7.12	7.12	90	120.05	P1	2.41	1.53	-
OOH*_PtS2	7.05	7.12	90	119.73	P1	2.41	1.88	-
O*_OH*_PtS2	7.19	7.17	90	120.90	P1	2.41	1.58	1.68
O*_PtS2	7.08	7.08	90	120	P1	2.41	1.54	-
OH*_PtS2	7.13	7.04	90	119.35	P1	2.42	1.73	-

The other way is known as the dissociative path, in which the O=O bond breaks into two O atoms on the active site of the catalytic surface. In this mechanism, after the dissociation of the O_2 , a sequence of reactions involves the addition of an electron-proton pair to the intermediates, leading to the following conversion: $2O^* \rightarrow O^*_OH^* \rightarrow O^* \rightarrow OH^* \rightarrow *$ (active site of the catalyst). In the final reaction step of the dissociation pathway, the catalyst is returned to its initial state, thereby enabling the ORR process to continue.

Both reaction pathways have been considered in this work by computing the value of adsorption energy (ΔE) for all the intermediates involved. The optimized structures of all the intermediates formed during both pathways are modelled using the VESTA software and are depicted in Figure 5.5. The corresponding lattice parameters and other various structural characteristics have been listed in Table 5.2.

Discussion of the various reaction steps involved in the **four-electron associative** ORR process:

Step 1: The adsorption of the O_2 molecule onto one of the catalytically active S atoms of the 2D monolayer PtS₂ is the first and common step of the ORR for both the associative and the dissociative pathway. For this reaction step, an O_2 molecule was placed on the top of the S atom of the 2D monolayer PtS₂, and then this structure was fully relaxed using the DFT-D3 approach. The equilibrium structure of the O_2^* _PtS₂ is shown in Figure 5.5 (a), having the average Pt-S bond distance and S-O bond distance as 2.42 Å and 2.78 Å, respectively. The adsorption energy (Δ E) for this reaction step is found to be 1.23 eV and is significantly positive, which indicates the endothermic nature of the reaction step. For this reaction step to occur, we need to apply an external potential that further facilitates the subsequent reaction steps of the ORR.

Step 2: In the next step of the 4e⁻ associative pathway, an electron and a proton from the anodic side reach the cathodic side and react with the adsorbed O₂ molecule on the 2D monolayer PtS₂ surface (i.e., with the O₂*_PtS₂ system). This leads to the formation of the OOH* intermediate, and the OOH*_PtS₂ system was fully relaxed using the same DFT-D3 method. The relaxed structure is represented in Figure 5.5 (b), having the average Pt-S bond length and S-O bond distance as 2.41 Å and 1.88 Å, respectively.

Step 3: In this step, the reduction of the OOH* intermediate to the O* intermediate takes place. In this reaction step, another pair of an electron and a proton from the anodic side combines with the OOH*_PtS₂ intermediate system, forming the O* intermediate with the evolution of the H₂O molecule, thereby reducing the OOH*_PtS₂ system to the O*_PtS₂ system. The relaxed geometry is shown in Figure 5.5 (d), and the average Pt-S bond length and S-O bond distance are 2.41 Å and 1.54 Å, respectively.

Step 4: Again, an electron-proton pair combines with the O*_PtS₂ intermediate, and as a result of this reaction step, the O*_PtS₂ intermediate system is converted to the OH*_PtS₂ intermediate system. The average Pt-S bond length and S-O bond distance are 2.42 Å and 1.73 Å, respectively, and the corresponding relaxed geometry is shown in Figure 5.5 (e).

Step 5: In the last step of this mechanism of the ORR process, the reduction of the OH*_PtS₂ intermediate system occurs by reacting with an electron-proton pair coming from the anodic side of the fuel cell. This leads to the formation of another H₂O molecule, which then simultaneously gets desorbed, and the catalyst is returned to its initial state (i.e., PtS₂) and becomes available to catalyze further ORR processes. In this way, we can see that the four-electron ORR occurs through the direct transfer of the four electrons, reducing the oxygen to water.

Discussion of the various reaction steps involved in the **four-electron dissociative** ORR process:

Step 1: Both the associative and dissociative pathways have the same initial step i.e., the adsorption of the O₂ molecule on the catalytically active S site of the 2D monolayer PtS₂. This step has already been explained in the 4e⁻ associative mechanism of the ORR process.

Step 2: In the second step of the 4e⁻ dissociative mechanism, the adsorbed O₂ molecule is dissociated into two individual oxygen atoms, and one of the O atoms gets migrated to a different catalytic site. The intermediate so formed is denoted by the 2O*_PtS₂ system and is represented in Figure 5.5 (b). The average Pt-S bond length and S-OH bond length in the relaxed structure are 2.41Å and 1.53Å, respectively.

Step 3: In the third step of the 4e- dissociative mechanism, the addition of a pair of a proton and an electron to one of the individual oxygen atoms bonded to the S atoms takes place when an electron and a proton come from the anodic side and combine with the 2O*_PtS₂ system. This leads to the formation of the O*_OH*_PtS₂ intermediate structure, and the corresponding equilibrium structure of the given system has been shown in Figure 5.5 (d). The average Pt-S bond length, S-O bond length, and S-OH bond length are 2.41 eV, 1.58 eV, and 1.68 eV, respectively.

Step 4: Further addition of another pair of a proton and an electron to the OH* intermediate of the O*_OH*_PtS₂ system leads to the desorption of the water molecule so formed, and the system reduces to O*_PtS₂. The properties of the O*_PtS₂ intermediate have already been mentioned in the above discussion of the associative

mechanism. After this reaction step, all the subsequent reaction steps are the same as the associative mechanism following the O^* _PtS₂ intermediate system.

5.2: ORR Catalytic Activity

In this work, we investigated the catalytic activity of the 2D monolayer PtS_2 by calculating the adsorption energy (ΔE) value for all the reaction steps involved in both reaction pathways using the same DFT-D3 theory. The first step of the ORR is the adsorption of the O_2 molecule on the 2D monolayer PtS_2 surface. The adsorption energy for the first step of the ORR is found to be positive, with a value of 1.43 eV. This implies that the binding of the O_2 molecule is an endothermic and energetically unfavorable process, and external energy must be supplied for the adsorption to occur. In the next step of the associative mechanism, the addition of a proton and an electron to the O_2^* _ PtS_2 system converts it into the OOH^* _ PtS_2 system, and this reaction step has negative adsorption energy, which indicates the exothermic nature of the reaction. The

Table 5.3. Adsorption energies (ΔE) for each ORR step of 2D monolayer PtS₂ in the associative pathway.

Reaction steps occurring during the associative pathway	Adsorption Energy (eV), ΔE	Relative Adsorption Energy
$PtS_2 + O_2 \rightarrow O_2^* - PtS_2$	1.43	1.43
O_2^* _PtS ₂ + H ⁺ + e ⁻ \rightarrow OOH [*] _PtS ₂	-1.12	0.31
$OOH^*_PtS_2 + H^+ + e^- \rightarrow O^*_PtS_2 + H_2O$	-3.06	-2.74
$O^*_{PtS_2} + H^+ + e^- \rightarrow OH^*_{PtS_2}$	-0.08	-2.82
$OH^*_PtS_2 + H^+ + e^- \rightarrow PtS_2 + H_2O$	-2.15	-4.96
(a)	(b)	
O ₂ * O ₂ * O ₀ * O ₀ * O ₀ * O ₀ * OH* -2.74eV -2.82eV -4.96eV	Relative Adsorption Energy (eV)	O*_OH* -0.99eV O*_OH* -2.74eV_2.82eV H2O -4.96eV
Reaction Coordinate (Associative Pathway)		ion Coordinate ciative Pathway)

Figure 5.6. Relative adsorption energy diagram at the surface of the 2D monolayer PtS_2 for (a) associative and (b) dissociative pathways during the ORR.

adsorption energy value of -1.12 eV lies in the optimum range as this indicates neither too strong nor too weak binding. An optimal adsorption energy ensures that the intermediates are bound strongly enough to facilitate the reaction but weak enough to allow for efficient desorption, enabling more continuous catalytic cycles. In the subsequent reaction step, the addition of another pair of an electron and a proton to the OOH* intermediate leads to the formation of the O* PtS₂ system and the evolution of a water molecule with an adsorption energy of -3.06 eV for the process. The large negative value of the adsorption energy for this reaction step implies that the intermediate O* is strongly bound to the catalytic surface. Thus, this intermediate will remain strongly bound to the catalyst, obstructing subsequent reaction steps. This strong binding thus can reduce the efficiency of the catalyst and the fuel cell. In the next step of the fourelectron associative ORR, the addition of another pair of an electron and a proton to the O* intermediate yields an OH* intermediate with an adsorption energy of -0.08 eV. This indicates the exothermic nature of the reaction step, and the process is energetically favorable. In the last step of the associative ORR mechanism, the addition of an electron and a proton again takes place to the OH* intermediate, yielding a water molecule and making the catalyst return to its initial state to assist more ORR cycles.

In comparison to the associative pathway, the dissociative pathway exhibits a more negative adsorption energy value of -1.82 eV for the reaction step O_2^* _PtS₂ \rightarrow $2O^*$ _PtS₂. The negative value indicates the exothermic nature of the reaction step, implying that the process is energetically favorable. In the next step of the four-electron

Table 5.4. Adsorption energies (ΔE) for each ORR step of 2D monolayer PtS₂ in the dissociative pathway.

Reaction steps occurring during the dissociative pathway	Adsorption Energy (eV), ΔE	Relative Adsorption Energy (eV)
$PtS_2 + O_2 \rightarrow O_2^* PtS_2$	1.43	1.43
O_2^* _PtS ₂ \rightarrow 20 * _PtS ₂	-1.82	-0.38
$2O^*_PtS_2 + H^+ + e^- \rightarrow O^*_OH^*_PtS_2$	-0.61	-0.99
$O^*_OH^*_PtS_2 + H^+ + e^- \rightarrow O^*_PtS_2 + H_2O$	-1.75	-2.74
$O^*_PtS_2 + H^+ + e^- \rightarrow OH^*_PtS_2$	-0.08	-2.82
$OH^*_PtS_2 + H^+ + e^- \rightarrow PtS_2 + H_2O$	-2.15	-4.96

dissociative pathway, the addition of an electron-proton pair to the 20* intermediate leads to the formation of the O*_OH* intermediate with the adsorption energy -0.61 eV. This reaction step is exothermic in nature, implying it is energetically favorable. The successive addition of another pair of a proton and an electron to the O*_OH* intermediate leads to the formation of the O* intermediate with the desorption of a water molecule and has a negative adsorption energy value of -1.75 eV. Again, this reaction step is exothermic in nature and is energetically favorable. The O* intermediate, on the successive addition of a proton and an electron, changes to the OH* intermediate. This reaction step has a negative adsorption energy of -0.08 eV, which implies that the reaction step is energetically favorable. The last step of this mechanism involves the addition of another pair of a proton and an electron to the OH* intermediate, causing the catalyst to return to its initial state. This reaction step has a negative adsorption energy of -2.15 eV, which means that the reaction step is exothermic in nature and the process is energetically favorable.

The tabular representation of the adsorption values of all the reaction steps for both associative and dissociative pathways is given in Tables 5.3 and 5.4, respectively. For the calculation of relative adsorption energies, the 2D monolayer PtS₂ was used as the reference geometry, with its energy set to 0 eV. The relative adsorption energies for each reaction step in both the associative and the dissociative ORR pathways are presented in Tables 5.3 and 5.4, respectively. The relative adsorption energy curves for both the associative and dissociative paths have been constructed by using the calculated relative adsorption energy values and are shown in Figure 5.6 (a) and (b), respectively. The total relative adsorption energy for both ORR mechanisms is calculated by summing the adsorption energies of all the reaction steps involved in the process and is found to be 4.96 eV for both the ORR pathways, which is sufficiently close to the reference value of -4.92 eV in a four-electron ORR process.

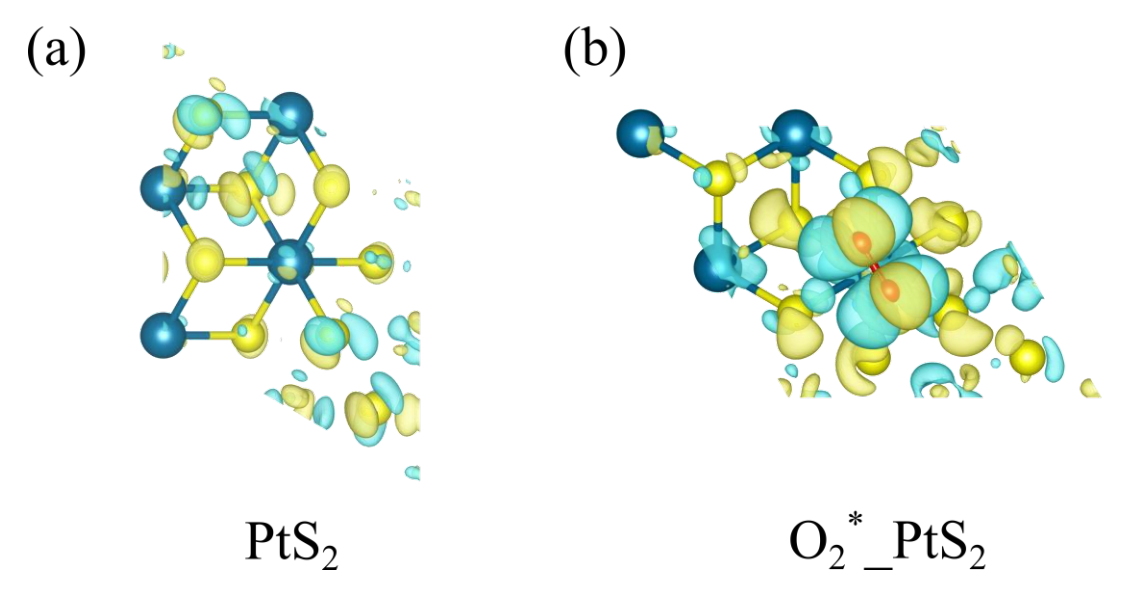


Figure 5.7. Spin-density plot for the (a) PtS₂ and (b) O₂* PtS₂.

In electrocatalysts, the electron density clouds are essential for enabling electron transfer and contributing to the reaction processes involved in the ORR. They help transfer electrons from the surface of the electrode to the O₂ molecules, as illustrated in Figure 5.7, where the yellow color represents the charge accumulation, and the cyan color represents the charge depletion. The interaction of the oxygen molecules with the electrocatalyst surface causes a shift in the electron density, affecting the oxygen molecule as well as the catalyst.

In summary, the catalytic performance of the 2D monolayer PtS_2 for the ORR was evaluated by plotting and analyzing the relative adsorption energy values for both reaction pathways. In constructing the potential energy curve, the 2D PtS_2 monolayer was used as the reference geometry, with its energy set to 0 eV for both the associative and dissociative pathways. Under standard conditions (pressure = 1 atm and temperature = 298.15 K), the expected value of the total relative adsorption energy value for the ORR, represented by $2H_2 + O_2 \rightarrow 2H_2O$, is -4.92 eV. The calculated total relative adsorption energy value was found to be -4.96 eV for both pathways, indicating that the total relative adsorption energy value derived from the DFT-D3 calculations aligns well with the reference value.

For the associative pathway, the adsorption energy value for the process $O_2^* \rightarrow OOH^*$ PtS₂ was found to be -1.12 eV, while the adsorption energy for the conversion O_2

 \rightarrow 20* for the dissociative pathway was -1.82 eV which is more negative, suggesting more exothermic nature and energetically favorability of the reaction step. As a result, the four-electron ORR process is more likely to proceed via the dissociative pathway.

Chapter 6: 2D monolayer Pt@PtS2

6.1: Structural and Electronic Properties

In this work, a 2×2 supercell of Pt atom anchored on the 2D monolayer PtS₂ (denoted by Pt@PtS₂) monolayer was designed by adding an extra Pt atom on the top of the chalcogen layer of the 2D monolayer PtS₂, serving as the catalytic site in the ORR mechanism. The 2×2 monolayer Pt@PtS₂ structure was optimized using the dispersion-corrected hybrid DFT (B3LYP-D3) method, and the top and side views of the equilibrium structure of the Pt atom anchored on the 2×2 monolayer PtS₂ are shown in Figure 6.1 (a) and (b), respectively. In this work, we have conducted spin-oriented computations to determine the equilibrium geometries, their electronic characteristics, and the energetics of the 2D monolayer Pt@PtS₂. These calculations accounted for the electron occupancy in the alpha (spin-up) and beta (spin-down) states to obtain a spin-polarized solution. The spin-polarized calculations were accomplished with the help of the keywords "ATOMSPIN" and "SPINLOCK" in the input file of the *ab initio* CRYSTAL23 suite program.

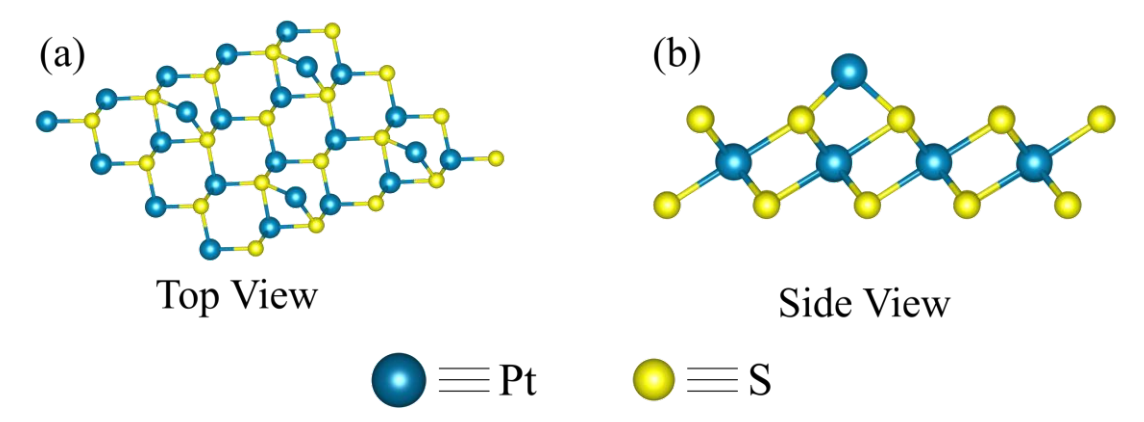


Figure 4. (a) Top view and (b) side view of the Pt atom anchored on the 2D monolayer PtS_2 ($Pt@PtS_2$).

The band structure and density of states (DOS) for the spin-up state of $Pt@PtS_2$ were studied along the highly symmetric Γ -M-K- Γ path with respect to the vacuum and are shown in Figure 6.2 (a) and (b), respectively. After the introduction of a Pt atom anchored on the 2D monolayer PtS_2 , the band gap is found to be an indirect band gap of 1.23 eV, reflecting a reduction from the initial band gap of 2.97 eV. This decrease in the band gap suggests the excellent electronic properties of the $Pt@PtS_2$ structure, which is

crucial for electrochemical processes like ORR and HER. Thus, Pt@PtS₂ may be a promising electrocatalyst for the ORR process.

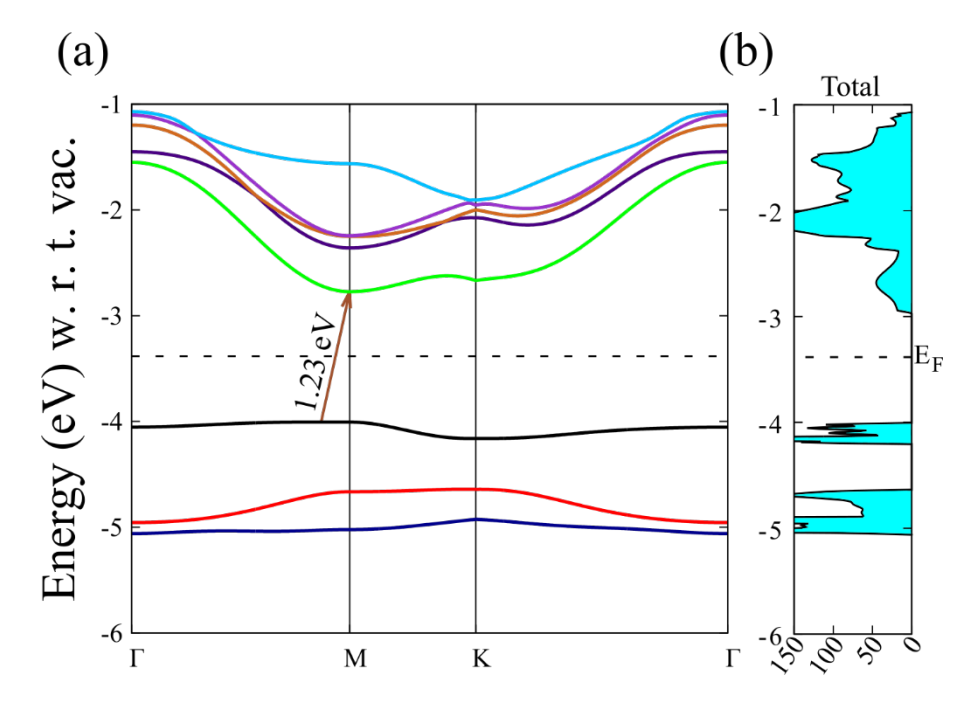


Figure 5. (a) Band structure and (b) DOS of the alpha spin Pt atom anchored on the 2D monolayer PtS₂ (Pt@PtS₂).

Subsequently, the analysis was extended to include both the spin-up and spin-down states and the corresponding band structure, and the DOS is shown in Figure 6.3 (a) and (b), respectively. In the Figure 6.3 (a), it can be clearly seen that both the alpha and beta spin bands are identical, which means there is no energy difference between the alpha and beta spin electrons at each corresponding *k*-point in the Brillouin zone i.e., the energy for the spin-up electrons is the same as that of the energy of the spin-down electrons at a given *k*-point of the Brillouin zone. As a result of the spin degeneracy, the DOS at any energy level is double that of the DOS of either the spin-up or the spin-down band, as shown in Figure 6.2 (b). The spin degeneracy of the Pt@PtS₂ can help facilitate better charge transfer, which is crucial in the ORR process and may lead to higher efficiency of the fuel cells.

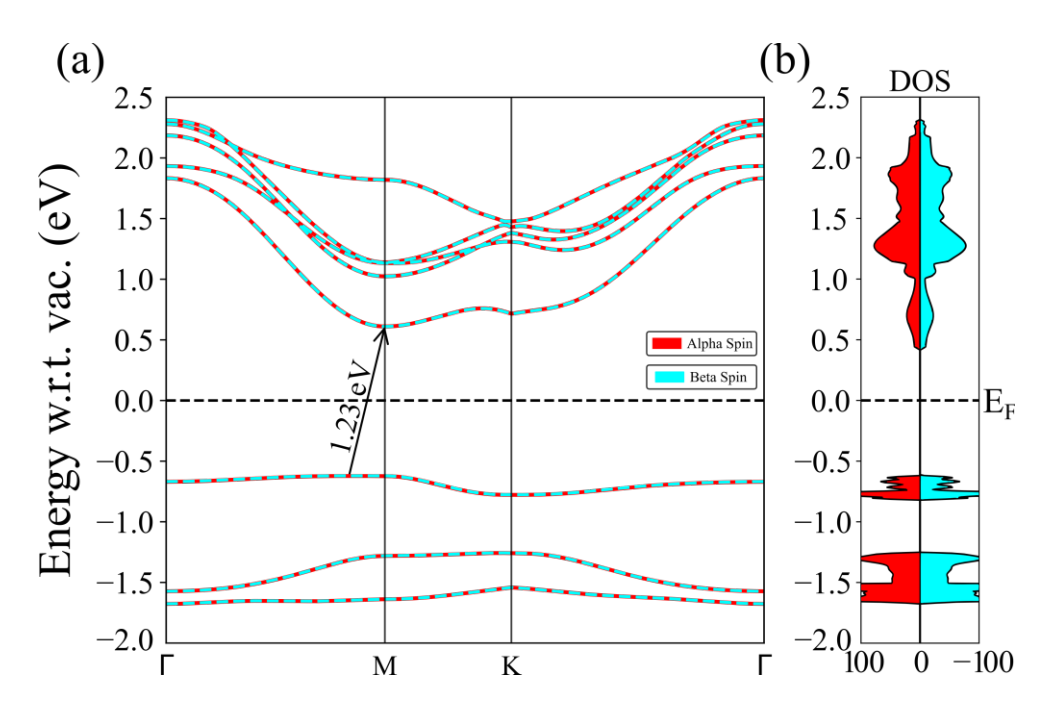


Figure 6. (a) Band structure and (b) DOS of both alpha and beta spins of the Pt atom anchored on the 2D monolayer PtS₂ (Pt@PtS₂).

The equilibrium structures of all the ORR intermediates for both reaction pathways are shown in Figure 6.4, and the corresponding lattice parameters, interfacial angle, and the required bond length data are listed in Table 6.1. The structures of all the intermediates have been modeled using the VESTA software. In the Pt@PtS₂, the anchored Pt atom acts as the prominent active catalytic site for the ORR. Table 6.1 includes all key properties, such as lattice parameters, interfacial angle, and bond lengths, for the 2×2 monolayer Pt@PtS₂ and all the ORR intermediates.

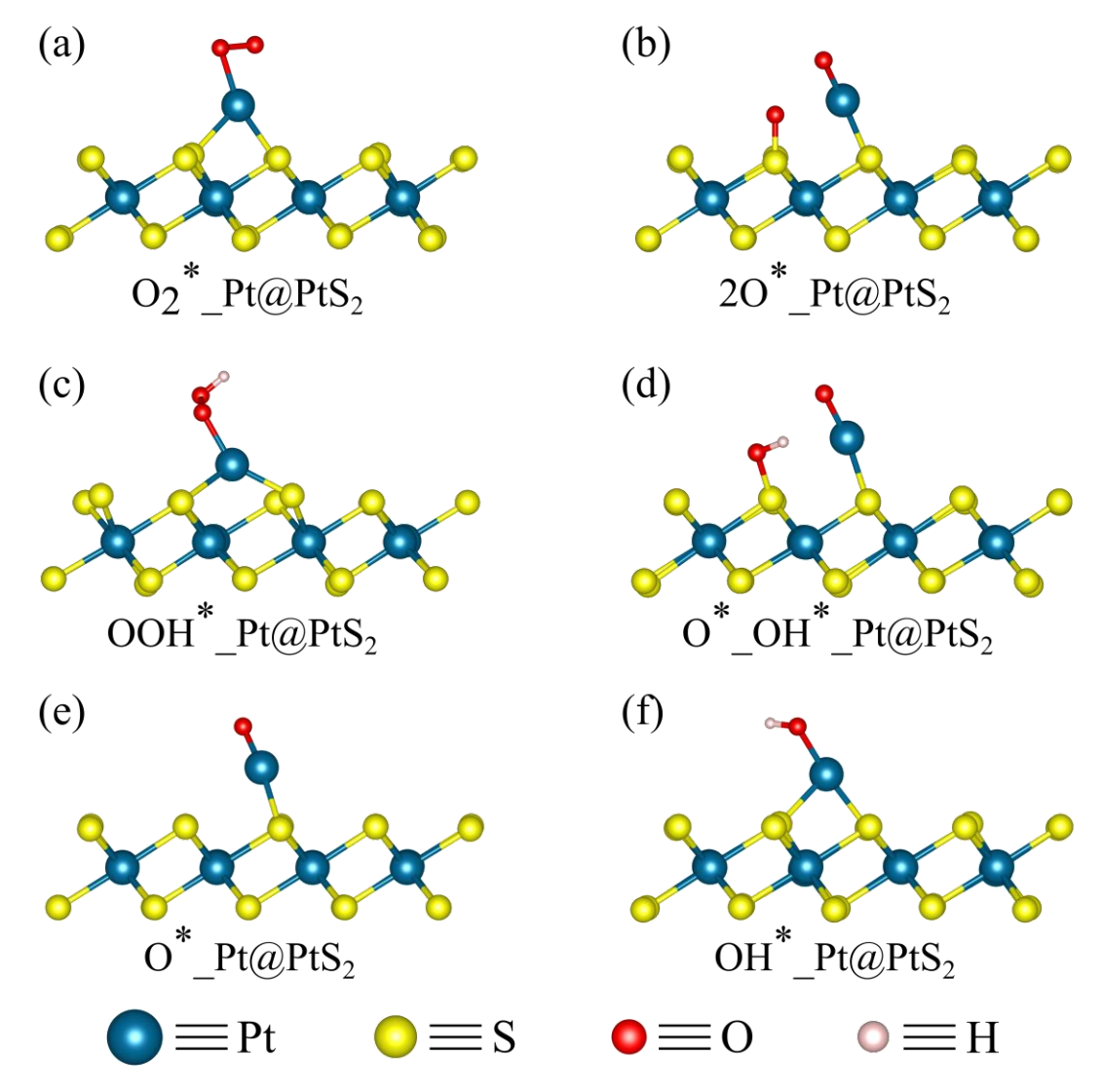


Figure 7. The side view of the equilibrium geometries of ORR intermediates of both pathways for 2D monolayer Pt@PtS₂.

Table 6.1. The equilibrium configuration of the intermediate structures of 2D monolayer $Pt@PtS_2$ during ORR.

Reaction Steps	Lat	tice	Interfa	cial angle	Symmetry	Avera	ge bond	length
	parameters (Å)			(°)			in Å	
-	a	b	α=β	γ	-	Pt-S	Pt-O	S-OH
2×2 Pt@PtS2	7.08	7.07	90	119.95	P1	2.44	-	-
O2*_Pt@PtS2	7.06	7.03	90	119.23	P1	2.41	2.06	-
2O*_Pt@PtS2	7.09	7.10	90	120.11	P1	2.41	1.80	-
OOH*_Pt@PtS2	7.05	7.14	90	118.87	P1	2.52	1.98	-
O*_OH*_Pt@PtS2	7.15	7.17	90	121.30	P1	2.41	1.80	1.72
O*_Pt@PtS2	7.06	7.07	90	120.02	P1	2.41	1.8	-

OH*_Pt@PtS2	7.05	7.02	90	119.15	P1	2.41	1.96	-	
-------------	------	------	----	--------	----	------	------	---	--

6.2: ORR Catalytic Activity

In this work, adsorption energy was calculated as the main parameter to examine the catalytic behavior of the system towards the ORR. We obtained the adsorption energy of each species involved in the associative and dissociative pathways using the B3LYP-D3 method, which has been listed in Tables 6.2 and 6.3, respectively. Additionally, we calculated the relative values of the adsorption energy for all the species by employing the 2D monolayer of Pt@PtS₂ as the reference geometry, with its energy defined as 0 eV for both the ORR pathways. The adsorption of the O₂ is a common step in both the paths, and has an adsorption energy of -1.70 eV, which indicates its exothermic nature, and thus the process is energetically favorable. In the next step of the associative mechanism, the addition of a proton and an electron coming from the anode side to the O₂* absorbed on the Pt@PtS₂ system takes place, and the adsorption energy calculated for this process is -0.63 eV, meaning that the process is exothermic, thereby indicating the possibility of the thermodynamic feasibility of the process. The calculated relative energy for the OOH* Pt@PtS2 system is found to be -2.33. The next step of the associative mechanism is again an exothermic process, wherein the addition of another pair of an electron and a proton to the OOH* intermediate adsorbed on the Pt@PtS₂ system leads to the formation of the O* Pt@PtS2 system. This process is accompanied by the removal of the water molecule formed due to the addition of a proton and an electron to the OH* and has an adsorption energy of -1.22 eV. The relative energy for this step is calculated to be -3.55 eV. The next step again includes the addition of an electron and a proton to the O* Pt@PtS₂ system to form the OH* Pt@PtS₂ system. This

Table 5.2. Adsorption energies (ΔE) for each ORR step in the associative mechanism for 2D monolayer Pt@PtS₂.

Reaction steps occurring during the associative pathway	Adsorption Energy (eV), ΔE	Relative Adsorption Energy (eV)
$Pt@PtS_2 + O_2 \rightarrow O_2^* Pt@PtS_2$	-1.70	-1.7
$O_2^* Pt@PtS_2 + H^+ + e^- \rightarrow OOH^* Pt@PtS_2$	-0.63	-2.33
$\frac{\text{OOH}^*_\text{Pt}@\text{PtS}_2 + \text{H}^+ + \text{e}^- \rightarrow \text{O}^*_\text{Pt}@\text{PtS}_2 + \\ \text{H}_2\text{O}}$	-1.22	-3.55
$O^*_Pt@PtS_2 + H^+ + e^- \rightarrow OH^*_Pt@PtS_2$	-1.85	-5.39
$OH^*_Pt@PtS_2 + H^+ + e^- \rightarrow Pt@PtS_2 + H_2O$	0.43	-4.96

step has an adsorption energy of -1.85 eV, which is an exothermic process and is energetically favorable. The last step is the addition of another pair of a proton and an electron to the OH* intermediate, and the catalyst is restored to its initial stage (i.e., Pt@PtS₂) with the evolution of another water molecule. The final step is the only step characterized by the positive adsorption energy with the value 0.43 eV.

Therefore, the final step of the associative ORR mechanism is an endothermic process, and external energy (potential) may be required to carry out the process. The relative adsorption energy value for all the species exhibits a decreasing trend in the potential energy surface for the associative pathway, except for the last step in which the catalyst is returned to its initial state, as shown in Figure 6.5 (a). This suggests strong catalytic activity of the 2D monolayer Pt@PtS2 towards the ORR mechanism at the Pt atom serving as the primary active site on the Pt@PtS2 surface. The adsorption energy for the last reaction step is small and positive, and this positive adsorption value is considerably small. Hence, this reaction step is unlikely to hinder the ORR mechanism occurring at the cathode of the fuel cell.

In the case of the dissociative pathway, two reaction steps of the ORR are associated with the positive adsorption energies, indicating that these processes are endothermic and, thus, energetically not favorable and thermodynamically less favorable.

Table 6.3. Adsorption energies (ΔE) for each ORR step in the dissociative pathway for 2D monolayer Pt@PtS₂.

Reaction steps occurring during the dissociative pathway	Adsorption Energy (eV), ΔE	Relative Adsorption Energy (eV)
$Pt@PtS_2 + O_2 \rightarrow O_2^* Pt@PtS_2$	-1.7	-1.7
O_2^* _Pt@PtS ₂ \rightarrow 2O*_Pt@PtS ₂	0.32	-1.38
$2O^*_Pt@PtS_2 + H^+ + e^- \rightarrow O^*_OH^*_Pt@PtS_2$	-0.70	-2.08
$O^*_OH^*_Pt@PtS_2 + H^+ + e^- \rightarrow O^*_Pt@PtS_2 + H_2O$	-1.47	-3.55
$O^*_Pt@PtS_2 + H^+ + e^- \rightarrow OH^*_Pt@PtS_2$	-1.85	-5.39
$OH^*_Pt@PtS_2 + H^+ + e^- \rightarrow Pt@PtS_2 + H_2O$	0.43	-4.96

The first step of these two reaction steps involves the dissociation of the O_2 into two adsorbed oxygen atoms, a process that may require energy input to overcome the bond cleavage barrier. This step has a positive adsorption energy of 0.32 eV, which is small but positive. The second step is the final step of the ORR, in which the adsorbed OH^*

intermediate species is converted back into the initial stage of the catalyst, accompanied by the formation and then the desorption of a water molecule. This step has a positive adsorption energy of 0.43 eV. The relative adsorption energies of all the ORR intermediates for the dissociative pathway are listed in Table 6.3. The remaining reaction steps of the dissociative pathway of the ORR exhibit negative adsorption energies, implying that those reaction steps are exothermic in nature and energetically favorable. The potential energy surface for the dissociative mechanism is shown in Figure 6.5 (b), in which we can see that two of the above-mentioned reaction steps show an uphill while the rest show a downhill. When compared with the associative pathway, it has been observed that only one step of the associative reaction mechanism exhibits positive adsorption energy. This indicates a lower overall energetic requirement for the progression of the reaction.

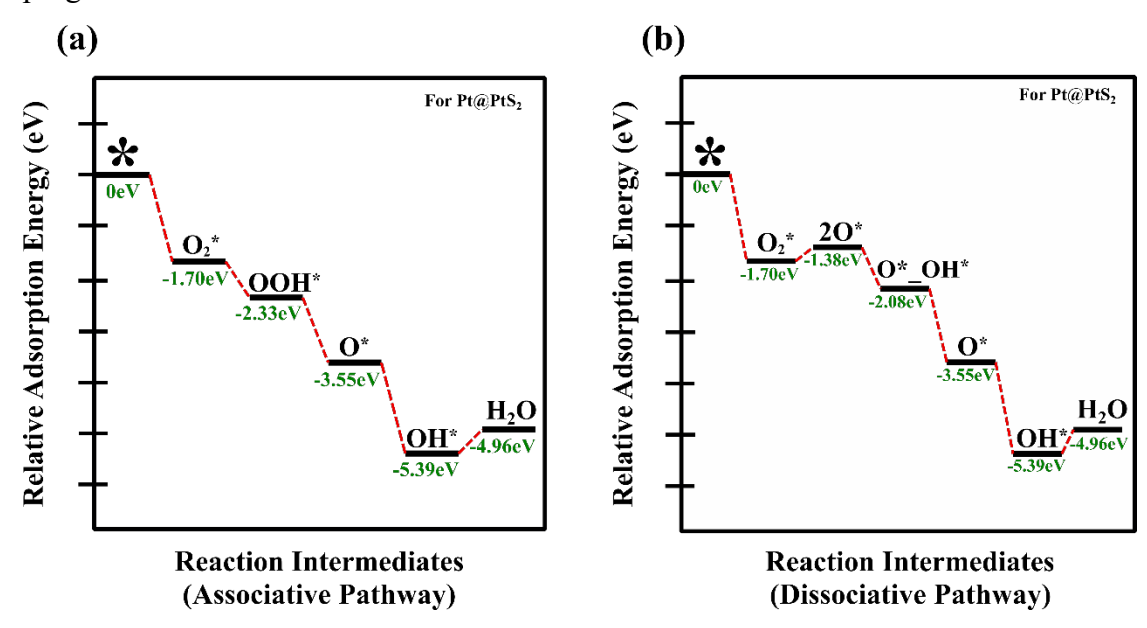


Figure 8. Relative adsorption energy diagram at the surface of the 2D monolayer Pt@PtS₂ for (a) associative and (b) dissociative pathways during the ORR.

Consequently, the associative pathway may be regarded as more favorable from the thermodynamics point of view and is, therefore, more likely to be preferred under comparable reaction conditions. Consequently, we can conclude that Pt@PtS₂ can be an excellent electrocatalyst during ORR.

Chapter 7: Conclusions and Future Goals

In this work, we conducted a computational investigation to analyze the structural and electronic properties and the catalytic activity of the 2D monolayer PtS₂ and Pt@PtS₂. We also examined the detailed mechanisms of the ORR on the surface of the 2D monolayer PtS₂ and Pt@PtS₂, exploring both the associative and dissociative pathways. This study concludes that the 1T phase of the 2D monolayer PtS2 has an octahedral coordination and a band gap of 2.97 eV, suggesting the semiconducting nature of the 1T-PtS₂. The 2H phase has a trigonal prismatic geometry and is metallic in nature. Considering the greater stability of the 1T-PtS₂, the ORR mechanism was explored exclusively for the 1T phase. To evaluate the catalytic performance for 1T-PtS₂, the adsorption energies (ΔE) of all the ORR intermediates were calculated for both pathways. The adsorption energy of the O₂* PtS₂ system is calculated to be 1.43 eV, indicating weak binding at the surface. As this step is common to both the ORR pathways, such high energy may limit the overall catalytic activity. Thus, we need to enhance the catalytic activity and the electronic properties of the 2D monolayer PtS₂. The adsorption energy for the conversion of the O_2^* PtS₂ system to the OOH* PtS₂ system is calculated to be -1.12 eV, while the conversion to the 20* PtS₂ system yields a more negative value of -1.82 eV. This indicates that the dissociative pathway is more exothermic, suggesting stronger and more stable binding of the intermediates to the catalytic surface. In contrast, the less negative adsorption energy value suggests the poor stability of the OOH*_PtS2 system as compared to the 2O* PtS2 system. Following this reaction step in both the ORR pathway, the relative adsorption energy for the subsequent reaction steps shows a downhill nature. As a result, the dissociative pathway is energetically more favorable and is thus expected to be thermodynamically preferred over the associative pathway for the 1T PtS₂.

In order to improve the electronic properties and catalytic activity of the PtS₂, a Pt atom was anchored on the chalcogen layer of the 2D monolayer PtS₂ surface (denoted by Pt@PtS₂). We further explored the structural properties, electronic properties, and catalytic activity of the Pt@PtS₂ towards the ORR process. It was found that Pt@PtS₂ possesses an indirect band gap of 1.23 eV, demonstrating its remarkable electronic

properties as compared to the 2D monolayer PtS₂ and thereby positioning it as a promising option as an electrocatalyst. We have explored both the associative and the dissociative mechanisms on the 2D monolayer Pt@PtS₂ surface. The adsorption energy for the adsorption of the O₂ on the 2D monolayer Pt@PtS₂ surface is found to be -1.70 eV, whereas for the 2D monolayer PtS₂ surface, it is a positive value of 1.43 eV. The difference between these two adsorption energies indicates a significant improvement in the catalytic activity after adding an anchored Pt atom onto the 2D monolayer PtS₂ surface.

The next step of the associative pathway after the formation of the O_2^* _Pt@PtS2 system is the addition of a pair of a proton and an electron to form the OOH*_Pt@PtS2 system. The adsorption energy for this reaction step is found to be -0.63 eV. The negative adsorption energy implies the exothermic nature of the reaction step, and the process is energetically favorable. On the contrary, the next step of the dissociation pathway after the formation of the O_2^* _Pt@PtS2 system is the breaking of the O_2 molecule into the two adsorbed oxygen atoms to form the $2O^*$ _Pt@PtS2 system. This reaction step has a positive adsorption energy of 0.32 eV, indicating that the process is energetically unfavorable.

The adsorption energies are found to be negative for the remaining steps of the ORR in both pathways, with an exception observed in the final step. In the final step, the OH*_Pt@PtS2 system gets converted into the initial state of the catalyst with the evolution of a water molecule. This step exhibits a small adsorption energy of 0.43 eV, which is energetically unfavorable, however, overcoming this energy barrier is not particularly challenging. Thus, based on the above analysis, the associative pathway of ORR is expected to be preferred energetically over the dissociative pathway on the surface of the 2D monolayer Pt@PtS2.

In addition to evaluating the ORR, it is equally important to examine the HER activity of the material, as a catalyst's bifunctional activity is crucial for enhancing the efficiency of the fuel cell. In this context, we will explore the HER process for the computationally designed 2D monolayer PtS₂ and 2D monolayer Pt@PtS₂ in the future.

REFRENCES

Abdelkareem M. A., Elsaid K., Wilberforce T., Kamil M., Sayed E. T., Olabi A. (2021), Environmental aspects of fuel cells: A review, Science of the Total Environment, 752, 141803 (DOI: 10.1016/j.scitotenv.2020.141803)

Back S., Kulkarni A. R., Siahrostami S. (2018), Single metal atoms anchored in two-dimensional materials: Bifunctional catalysts for fuel cell applications, ChemCatChem, 10, 3034–3039 (DOI: 10.1002/cctc.201800447)

Chen Z. Y., Yang J. L. (2006), The B3LYP hybrid density functional study on solids, Frontier of Physics in China, 3, 339–343 (DOI:10.1007/s11467-006-0026-8)

Chu S., Cui Y., Liu N. (2016), The path towards sustainable energy, Nature Materials, 16, 16–22 (DOI: 10.1038/nmat4834)

Dange P., Savla N., Pandit S., Bobba R., Jung S. P., Gupta P. K., Sahni M., Prasad R. (2022), A comprehensive review on oxygen reduction reaction in microbial fuel cells, Journal of Renewable Materials, 10, 665–697 (DOI: 10.32604/jrm.2022.015806)

Duan Z., Wang G. (2013), Comparison of reaction energetics for oxygen reduction reactions on Pt (100), Pt (111), Pt/Ni (100), and Pt/Ni (111) surfaces: A first-principles study, Journal of Physical Chemistry C, 117, 6284–6292 (DOI: 10.1021/jp400388v)

Epstein S. T., Rosenthal C. M. (1976), The Hohenberg-Kohn theorem, Journal of Chemical Physics, 64, 247-249 (DOI: 10.1063/1.431969)

Erba A., Desmarais J. K., Casassa S., Civalleri B., Donà L., Bush I. J., Searle B., Maschio L., Edith-Daga L., Cossard A., Ribaldone C., Ascrizzi E., Marana N. L., Flament J. P., Kirtman B. (2023), CRYSTAL23: A program for computational solid state physics and chemistry, Journal of Chemical Theory and Computation, 19, 6891–6932 (DOI: 10.1021/acs.jctc.2c00958)

Felseghi R. A., Carcadea E., Raboaca M. S., Trufin C. N., Filote C. (2019), Hydrogen fuel cell technology for the sustainable future of stationary applications, Energies, 12, 4593 (DOI: 10.3390/en12234593)

Gewirth A. A., Thorum M. S. (2010), Electroreduction of dioxygen for fuel-cell applications: Materials and challenges, Inorganic Chemistry, 49, 3557–3566 (DOI: 10.1021/ic9022486)

Grimme S., Antony J., Ehrlich S., Krieg H. (2010), A consistent and accurate ab initio parametrization of density functional dispersion correction (DFT-D) for the 94 elements H-Pu, Journal of Chemical Physics, 132, 154104 (DOI: 10.1063/1.3382344)

Harker A. H. (2016), Materials modelling using density functional theory: Properties and predictions, by Giustino Feliciano, Contemporary Physics, 57, 140-141 (DOI: 10.1080/00107514.2015.1100218)

Kartha S., Grimes P. (1994), Fuel cells: Energy conversion for the next century, Physics Today, 47, 54–61 (DOI: 10.1063/1.881426)

Hohenberg P., Kohn W. (1964), Inhomogeneous electron gas, Physical Review, 136, B864 (DOI: 10.1103/PhysRev.136.B864)

Hosseini S. H., Tsolakis A., Alagumalai A., Mahian O., Lam S. S., Pan J., Peng W., Tabatabaei M., Aghbashlo M. (2023), Use of hydrogen in dual-fuel diesel engines, Progress in Energy and Combustion Science, 98, 101100 (DOI: 10.1016/j.pecs.2023.101100)

Huang H. C., Li J., Zhao Y., Chen J., Bu Y. X., Cheng S. B. (2021), Adsorption energy as a promising single-parameter descriptor for single atom catalysis in the oxygen evolution reaction, Journal of Materials Chemistry A, 9, 6442–6450 (DOI: 10.1039/D0TA12567A)

Hussain S., Yangping L. (2020), Review of solid oxide fuel cell materials: Cathode, anode, and electrolyte, Energy Transitions, 4, 113–126 (DOI: 10.1007/s41825-020-00029-8)

Kulkarni T., Slaughter G. (2015), Enzymatic glucose biofuel cell and its application, Journal of Biochips & Tissue Chips, 5, 1000111 (DOI: 10.4172/2153-0777.1000110)

Kumbhakar P., Jayan J. S., Sreedevi Madhavikutty A., Sreeram P. R., Saritha A., Ito T., Tiwary C. S. (2023), Prospective applications of two-dimensional materials beyond laboratory frontiers: A review, iScience, 26, 106671 (DOI: 10.1016/j.isci.2023.106671)

Maheshwari K., Sharma S., Sharma A., Verma S. (2018), Fuel cell and its applications: A review, International Journal of Engineering Research & Technology (IJERT), 7, 6–9.

Mekhilef S., Saidur R., Safari A. (2012), Comparative study of different fuel cell technologies, Renewable and Sustainable Energy Reviews, 16, 981–989 (DOI: 10.1016/j.rser.2011.09.020)

Momma K., Izumi F. (2011), VESTA 3 for three-dimensional visualization of crystal, volumetric and morphology data, Journal of Applied Crystallography, 44, 1272–1276, (DOI: 10.1107/S0021889811038970)

Monkhorst H. J., Pack J. D. (1976), Special points for Brillouin-zone integrations, Physical Review B, 13, 5188–5192 (DOI: 10.1103/PhysRevB.13.5188)

Nie Y., Li L., Wei Z. (2015), Recent advancements in Pt and Pt-Free catalysts for oxygen reduction reaction, Chemical Society Reviews, 44, 2168–2201 (DOI: 10.1039/C4CS00484A)

Nørskov J. K., Rossmeisl J., Logadottir A., Lindqvist L., Kitchin J. R., Bligaard T., Jónsson H. (2004), Origin of the overpotential for oxygen reduction at a fuel-cell cathode, Journal of Physical Chemistry B, 108, 17886–17892 (DOI: 10.1021/jp047349j)

Owusu P. A., Asumadu-Sarkodie S. (2016), A review of renewable energy sources, sustainability issues and climate change mitigation, Cogent Engineering, 3, 1167990 (DOI: 10.1080/23311916.2016.1167990)

Rosli N. F., Mayorga-Martinez C. C., Latiff N. M., Rohaizad N., Sofer Z., Fisher A. C. Pumera M. (2018), Layered PtTe₂ matches electrocatalytic performance of Pt/C for oxygen reduction reaction with significantly lower toxicity, ACS Sustainable Chemistry and Engineering, 6, 7432–7441 (DOI: 10.1021/acssuschemeng.7b04920)

Singh A., Pakhira S. (2023), Unraveling the electrocatalytic activity of platinum doped zirconium disulfide toward the oxygen reduction reaction, Energy and Fuels, 37, 567–579 (DOI: 10.1021/acs.energyfuels.2c02831)

Singh A., Pakhira S. (2024), Synergistic niobium doped two-dimensional zirconium diselenide: An efficient electrocatalyst for O₂ reduction reaction, ACS Physical Chemistry Au, 4, 40–56 (DOI: 10.1021/acsphyschemau.3c00035)

Sun H., Gao L., Li Y., Xu Q., Li Y., Liu W. (2025), Screening of single-atomic catalysts loaded on two-dimensional transition metal dichalcogenides for electrocatalytic oxygen reduction via high throughput ab initio calculations, Journal of Colloid and Interface Science, 684, 251–261 (DOI: 10.1016/j.jcis.2025.01.060)

Tosoni S., Tuma C., Sauer J., Civalleri B., Ugliengo P. (2007), A comparison between plane wave and gaussian-type orbital basis sets for hydrogen bonded systems: formic acid as a test case, Journal of Chemical Physics, 127, 154102 (DOI:10.1063/1.2790019)

Upadhyay S. N., Pakhira S. (2021), Mechanism of electrochemical oxygen reduction reaction at two-dimensional Pt-doped MoSe₂ material: An efficient electrocatalyst, Journal of Materials Chemistry C, 9, 11331–11342 (DOI: 10.1039/D1TC02193A)

Vilela Oliveira D., Laun J., Peintinger M. F., Bredow T. (2019), BSSE-correction scheme for consistent gaussian basis sets of double- and triple-zeta valence with polarization quality for solid-state calculations, Journal of Computational Chemistry, 40, 2364–2376 (DOI: 10.1002/jcc.26013)

Yin S., Luo Q., Wei D., Guo G., Sun X., Tang Y., Dai X. (2022), A type-II PtS₂/MoTe₂ van der Waals heterostructure with adjustable electronic and optical properties, Results in Physics, 33, 105172 (DOI: 10.1016/j.rinp.2021.105172)